OXFORD

Journal of Petrology, 2024, **65**, egae028
https://doi.org/10.1093/petrology/egae028
Advance access publication date 8 March 2024
Original Manuscript

The Role of Crustal Contamination throughout the 1329–2005 CE Eruptive Record of Mt. Etna Volcano, Italy

Marie K. Takach [1,2,*], Wendy A. Bohrson[1,3], Frank J. Spera[4] and Marco Viccaro [5,6]

[1]Current address: Department of Geological Sciences, Central Washington University, Ellensburg, WA 98926, USA
[2]College of Earth, Ocean, and Atmospheric Sciences, Oregon State University, Corvallis, OR 97311, USA
[3]Current address: Department of Geology and Geological Engineering, Colorado School of Mines, Golden, CO 80401, USA
[4]Department of Earth Science and Earth Research Institute, University of California, Santa Barbara, CA 93106, USA
[5]Department of Biological, Geological, and Environmental Sciences, University of Catania, Catania, Italy
[6]Istituto Nazionale di Geofisica e Vulcanologia - Sezione di Catania, Osservatorio Etneo, Catania, Italy

*Corresponding author. E-mail: marie.takach@gmail.com

The nearly continuous volcanic eruption record at Mt. Etna dating back ~700 years provides an excellent opportunity to investigate the geochemical evolution of a highly active volcano. Of particular interest is elucidating the cause of selective enrichment in alkali elements (K and Rb) and $^{87}Sr/^{86}Sr$ observed in various episodes of past activity. More recently, this alkali enrichment trend started to manifest in the 17th century and accelerated after 1971, and was accompanied by an increase in the volume, frequency, and explosivity of eruptions. Explanations for this signature include recharge of alkali-enriched magmas and/or crustal contamination from the subvolcanic basement. This study quantitatively examines the role of crustal contamination in post-1971 Etnean magma compositions *via* hundreds of open-system phase equilibria and trace element calculations based upon whole-rock major oxides, trace elements, $^{87}Sr/^{86}Sr$ ratios, and mineral compositional data. Available pre-1971 petrochemical data are satisfactorily reproduced by fractional crystallization of a high whole-rock MgO (12–17 wt.%), Ni (135–285 ppm), and Cr (920–1330 ppm) parental magma composition that is documented in Etna's ~4-ka fall-stratified deposit. Observed post-1971 whole-rock and glass trends and phase equilibria are reproduced *via* modeled assimilation of a skarn and flysch mixture, lithologies that represent the uppermost 10 to 15 km of sedimentary rocks beneath Etna. Notably, models show that K_2O (wt.%) and Rb (ppm) behave incompatibly during partial melting of skarn/flysch. Additionally, the observed elevation of $^{87}Sr/^{86}Sr$ in post-1971 samples is consistent with the addition of radiogenic Sr from wallrock partial melts. In best-fit models, which yield observed post-1971 K_2O, Rb, and $^{87}Sr/^{86}Sr$ trends, ~17% anatectic melt is assimilated and there may be a subordinate stoped wallrock component of ≤2% (percentage is relative to the starting mass of pristine magma). Previous work has shown that metasomatized spinel lherzolite and garnet pyroxenite can be melted in different proportions to reproduce long- and short-term changes observed in Etna's geochemical products. We propose that the alkali enrichment signature observed after 1971 can be fully explained through the combination of mantle heterogeneity and crustal contamination. In particular, up to ~20% crustal input coupled with mantle heterogeneity of primitive melts explains the geochemical signals quite well. The influence of crustal contamination on post-1971 lavas is, in part, the result of frequent recharge of magmas that thermally primed the middle to upper crust and enhanced its partial melting.

Key words: Mt. Etna; crustal contamination; assimilation; thermodynamic modeling; Magma Chamber Simulator

INTRODUCTION

Mt. Etna is a largely trachybasaltic stratovolcano that developed since ~500 ka on what is now the densely populated coast of eastern Sicily, Italy (Figs. 1 and 2a), and is among the most active and well-monitored volcanoes in the world (Kahl *et al.*, 2011; Branca *et al.*, 2011a; Corsaro & Miraglia, 2014; Cannata *et al.*, 2018). Etna experienced a recent shift from sodic to potassic affinity in its alkalic series (Fig. 2b) (Corsaro & Pompilio, 2004a) as well as Rb enrichment and more radiogenic $^{87}Sr/^{86}Sr$ (Fig. 2d-e) compared to earlier stages of magmatism. The alkali enrichment trend started in the 17th century and increased dramatically starting in the 1970s. Since then, lavas with the most radiogenic Sr isotopes and melts with the highest K concentrations ever produced at comparable differentiation degrees were emitted (Fig. 2c, e) (Tanguy & Kieffer, 1976; Tanguy & Clocchiatti, 1984; Barbieri *et al.*, 1993; Armienti *et al.*, 1994a, 2007; Condomines *et al.*, 1995; Tonarini *et al.*, 2001; Corsaro & Pompilio, 2004a). This geochemical signature is accompanied by a striking change in the volcano's eruptive behavior after 1971 with increases in the explosivity, frequency, and volume of eruptions. The alkali enrichment and accompanying eruptive activity shift at Etna remains a prevailing scientific problem.

Endmember ideas proffered to explain the alkali enrichment include: (1) crustal contributions in the form of alkali-rich fluids or melts (e.g. Clocchiatti *et al.*, 1988; Condomines *et al.*, 1995), and (2) changes to the mantle source delivered to the shallow plumbing system by mafic recharge (e.g. Tonarini *et al.*, 2001; Armienti *et al.*, 2007). A variable mantle source for Etna has been shown to produce compositional differences in Etna's erupted products' *via* resident magmas mixing with recharge magmas originating from a source that is either heterogenous (Armienti *et al.*, 1989; Barbieri *et al.*, 1993; Viccaro & Cristofolini, 2008; Corsaro & Métrich, 2016; Viccaro & Zuccarello, 2017), has been partially melted to different degrees (Clocchiatti *et al.*, 1998) or in varied proportions (Casetta *et al.*, 2019), and/or metasomatized

Received: July 24, 2023. **Revised:** January 29, 2024. **Accepted:** March 4, 2024

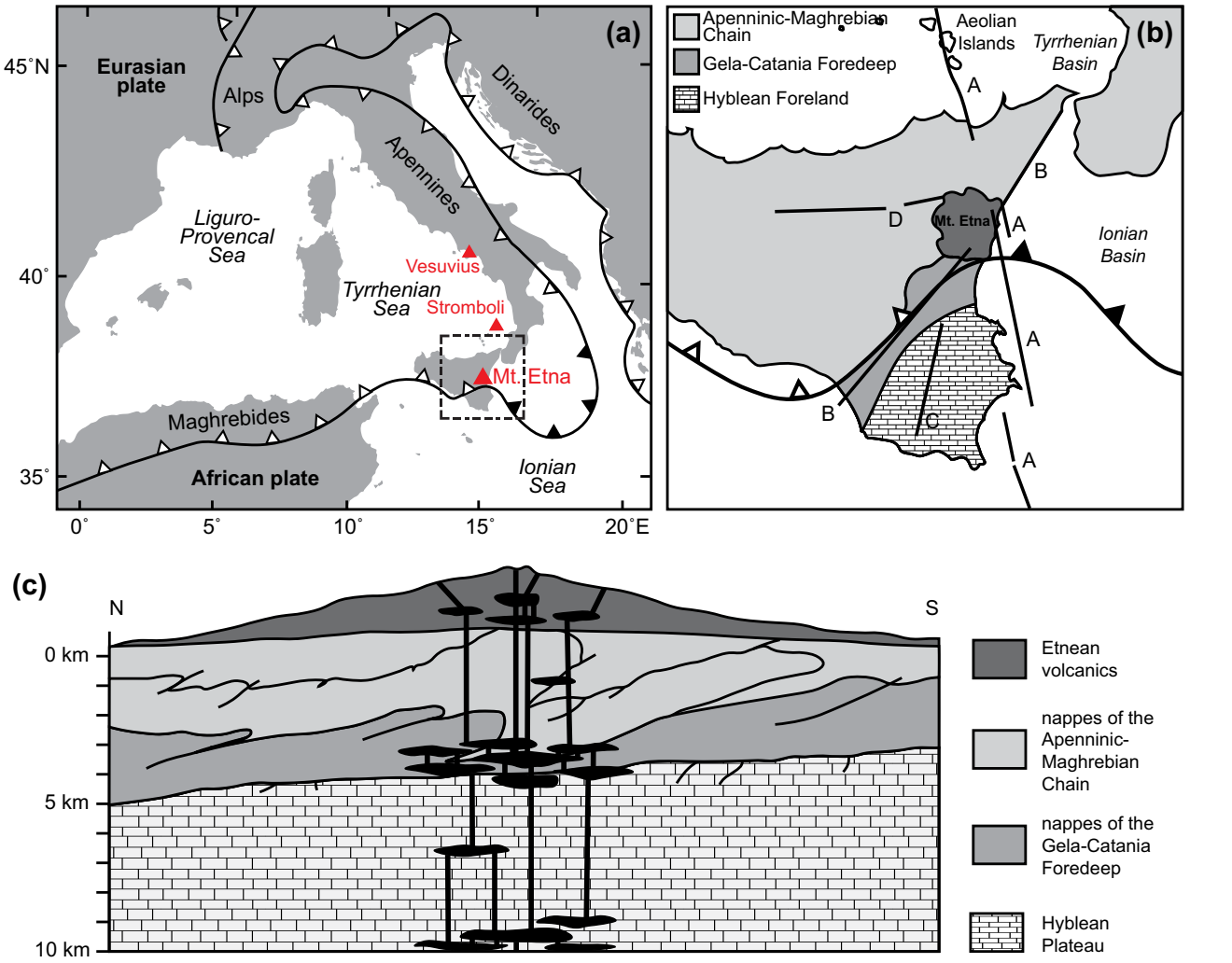

Fig. 1. Geological setting of Etna. (**a**) Regional tectonic setting of the western Mediterranean including Etna. Black triangles: oceanic lithosphere subduction; open triangles: continent-continent collision; bold type: tectonic plates; italic type: sea basins; regular type: mountain ranges. Redrawn after Schellart (2010). (**b**) Simplified map illustrating Etna's position at the intersection of two tectonic domains: (1) the orogenic domain to the N-NW composed of the Apenninic-Maghrebian Chain, and (2) the foreland domain to the S-SE composed of the Gela-Catania foredeep, Hyblean foreland, and Ionian basin (tectonic domains redrawn after Catalano *et al.*, 2004). Major fault systems: A, Aeolian-Maltese; B, Comiso-Messina; C, Scicli; D, Monte Kumeta-Alcantara (faults redrawn after Bousquet & Lanzafame, 2004). **(c)** Schematic crustal section beneath Etna highlighting the sedimentary basement (redrawn after Grasso & Lentini, 1982 and Lentini, 1982).

by carbonatite (Bragagni *et al.*, 2022) or subduction-related fluids from the adjacent Ionian slab (Schiano *et al.*, 2001; Tonarini *et al.*, 2001; Armienti *et al.*, 2004). For example, Viccaro & Zuccarello (2017) propose that variable metasomatism of the mantle source, changing degrees of partial melting of lherzolite and pyroxenite, and magma mixing can account for some of Etna's temporal geochemical variations, whereas Casetta *et al.* (2019) suggest varied proportions of amphibole and phlogopite melting in the source linked to heterogenous H_2O and CO_2 activity drives Etna's geochemical changes. Regardless of the exact mantle source, magma mixing has been an important process during at least the last ~700 years (La Delfa *et al.*, 2001; Clocchiatti *et al.*, 2004; Viccaro *et al.*, 2006, 2010, 2015; Armienti *et al.*, 2007; Corsaro *et al.*, 2009; Ferlito *et al.*, 2009, 2012; Andronico & Corsaro, 2011; Kahl *et al.*, 2011, 2013, 2017; Corsaro & Miraglia, 2014; Giacomoni *et al.*, 2016; Giuffrida & Viccaro, 2017; Ubide & Kamber, 2018; Salem *et al.*, 2019; Magee *et al.*, 2021 and more). Furthermore, Etna has been active for decades, with recent volcanic activity increasing in volume and frequency (Branca & Del Carlo, 2004, 2005), which likely implies the replenishment of magma chambers from deeper reservoirs in the lower crust or mantle.

The wide array of previous works demonstrates the importance of magma recharge and mixing to produce the spectrum of erupted products at Etna. Still, other proponents argue that carbonate/flysch basement assimilation also contributes to the changing geochemical signature in Etnean magmas (e.g. Clocchiatti *et al.*, 1988; Condomines *et al.*, 1995; Tanguy *et al.*, 1997). These subvolcanic sedimentary strata are ≤15 km thick and composed of variable carbonates, shales, siltstones, and sandstones. Collectively, these crustal lithologies are rich in alkali elements with relatively high $^{87}Sr/^{86}Sr$ (e.g. Clocchiatti *et al.*, 1988; Armienti *et al.*, 1989), providing a potential source of the alkali and $^{87}Sr/^{86}Sr$ enrichment observed.

Effects of carbonate assimilation at volcanoes with carbonate basements are extensively recognized, for example, in the following locations: the Colli Albani volcanic district (Iacono Marziano *et al.*, 2007; Freda *et al.*, 2008; Di Rocco *et al.*, 2012), Mt. Vesuvius (Del Moro *et al.*, 2001; Iacono Marziano *et al.*, 2008, 2009; Jolis *et al.*,

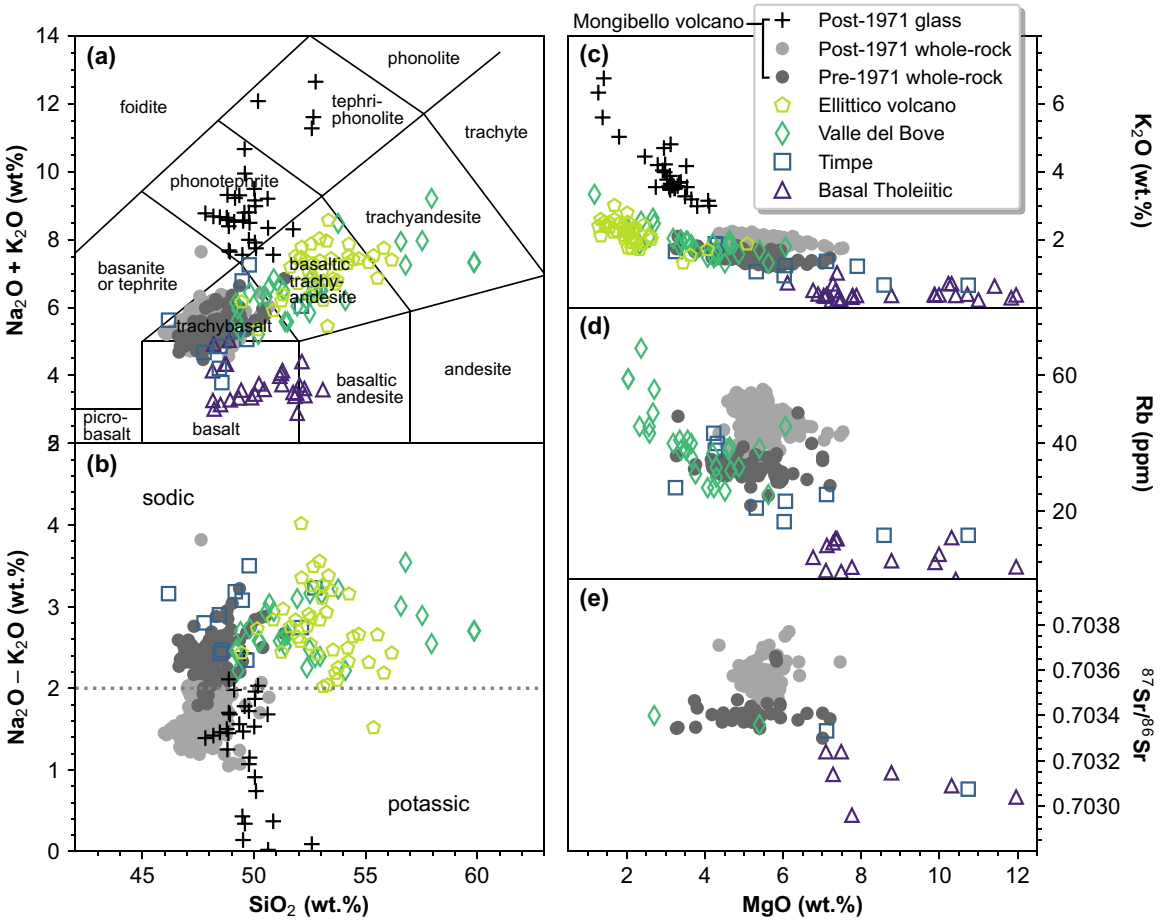

Fig. 2. Chemical variation diagrams illustrate the compositional diversity of lavas from each supersynthem in Etna's history, from oldest (Basal Tholeiitic) to youngest (Stratovolcano, represented by Ellittico and Mongibello volcanoes). (**a**) Total alkali-silica diagram (fields from Le Maitre, 1989). (**b**) Discrimination diagram between sodic and potassic affinities in alkalic series rocks (fields from Le Bas *et al.*, 1986). (**c-e**) Diagram showing MgO versus K_2O (wt.%), Rb (ppm), and $^{87}Sr/^{86}Sr$, respectively, for Etnean lavas. Note that post-1971 glasses exhibit the highest K_2O concentrations ever sampled from Etna. Data for the Basal Tholeiitic, Timpe, and Valle del Bove Supersynthems, and Ellittico volcano taken from GEOROC (Electronic Appendix 5). Data for the Mongibello volcano taken from the studies outlined in Electronic Appendix 1.

2015), and the Campi Flegrei volcanic district (Pappalardo *et al.*, 2002) in Italy, Merapi volcano in Indonesia (Chadwick *et al.*, 2007; Deegan *et al.*, 2010; Borisova *et al.*, 2013), and Popocatépetl volcano, Mexico (Goff *et al.*, 1998, 2001). Experimental and petrological studies document geochemical interactions between magma and carbonate rocks including (1) calc-silicate xenoliths with textures indicative of intense magmatic interaction, (2) highly radiogenic $^{87}Sr/^{86}Sr$ volcanic products suggestive of crustal input, (3) Ca-rich phases, and (4) large CO_2 releases from carbonate rocks (Michaud, 1995; Del Moro *et al.*, 2001; Chadwick *et al.*, 2007; Iacono Marziano *et al.*, 2008, 2009; Deegan *et al.*, 2010; Mollo *et al.*, 2010; Di Rocco *et al.*, 2012; Borisova *et al.*, 2013; Heap *et al.*, 2013; Jolis *et al.*, 2013). Gravity and deep dipole geoelectrics (Loddo *et al.*, 1989), structural interpretations (Borgia *et al.*, 1992), and stratigraphic relationships (Grasso & Lentini, 1982; Pedley & Grasso, 1992) provide documentation that at least the upper 10 to 15 km of crust on which Etna developed is composed of sedimentary rocks, and siliceous, peraluminous, and carbonate sedimentary xenoliths are documented at Etna (e.g. Clocchiatti *et al.*, 1988; Michaud, 1995; Lanzafame *et al.*, 2003; Neri *et al.*, 2004; Corsaro *et al.*, 2007; Coulson *et al.*, 2011). However, there are no extensive mass- and energy-constrained quantitative studies that examine the degree to which interactions between Etna's magmas and the sedimentary basement in which they reside can explain the post-1971 alkali enrichment signatures. That investigation is the main topic of this study with the use of Magma Chamber Simulator (Bohrson *et al.*, 2014, 2020; Heinonen *et al.*, 2020).

GEOLOGICAL BACKGROUND

At present, Etna reaches a maximum elevation of 3357 m a.s.l. with an ellipsoidal base covering 1250 km^2 (Patanè *et al.*, 2011). The island of Sicily upon which Etna developed lies near the center of the Mediterranean Basin, a region marked by complex tectonic and geodynamic features (Fig. 1a, b). Etna formed in an area of roughly north–south Neogene-Quaternary convergence of the African and Eurasian plates (Dewey *et al.*, 1989; Lentini *et al.*, 2006). Here, there are two primary tectonic domains: (1) the orogenic domain to the north composed of the Apenninic-Maghrebian Chain, and (2) the foreland domain to the south composed of the Gela-Catania foredeep, Hyblean foreland, and Ionian basin (Fig. 1b). Etna's magmatism is focused at the intersection of these domains, and the magma storage system is in the Sicilian continental crust where the Gela-Catania foredeep and Apenninic-Maghrebian chain meet (Cristofolini *et al.*, 1985; Bousquet & Lanzafame, 2004; Lentini *et al.*, 2006; Patanè *et al.*, 2011). The sedimentary basement beneath Etna is uplifted to 700 to 1300 m a.s.l. and capped by 2000 to 2600 m of Etna's volcanic

products (Catalano *et al.*, 2004); the lower 8 to 10 km are comprised of Hyblean Plateau carbonate rocks (Loddo *et al.*, 1989; Yellin-Dror *et al.*, 1997; Corsaro & Pompilio, 2004b) overlain by 2 to 5 km of varied carbonates, shales, siltstones, and sandstones including sequences of flysch from the Apenninic-Maghrebian chain and Gela-Catania foredeep nappes (Fig. 1c) (Lentini, 1982; Loddo *et al.*, 1989; Tibaldi & Groppelli, 2002; Bousquet & Lanzafame, 2004; Corsaro & Pompilio, 2004b).

Unconformity-bound stratigraphy emphasizes four major evolutionary phases, or 'supersynthems', of submarine transitioning to subaerial eruptive activity at Etna (De Beni *et al.*, 2011; Branca *et al.*, 2011a, 2011b). Following Branca *et al.* (2011a), these are Basal Tholeiitic (542–320 ka), Timpe (221–112 ka), Valle de Bove (106–65 ka), and Stratovolcano (Ellittico and Mongibello; <57 ka) (Fig. 2). Etna's alkalic series (Timpe and younger) is dominantly Na-alkalic except for post-1971 eruptive products with potassic affinity (Fig. 2b). Volcanics in the Stratovolcano phase range from alkali basalts to trachytes (Fig. 2a) and the most common products in the Ellittico and Mongibello volcanoes are mugearites and hawaiites, respectively. Plagioclase is the predominant phenocryst during this phase followed by clinopyroxene, olivine, and Ti-magnetite. Apatite is sometimes an accessory phase (Corsaro & Pompilio, 2004a), and Ca-amphibole and orthopyroxene are documented in select eruptions (Clocchiatti *et al.*, 2004; Viccaro *et al.*, 2006). For eruptions between 1329 and 2005 CE, lavas typically exhibit 10% to 40% by volume of phenocrysts (Armienti *et al.*, 1994a; Corsaro *et al.*, 2007, 2009; Viccaro & Cristofolini, 2008; Ferlito *et al.*, 2009; De Beni *et al.*, 2011), and rarely >40 vol% (Corsaro *et al.*, 1996; Nicotra & Viccaro, 2012; Kahl *et al.*, 2017). Etnean magmas often contain ~1 to 4 wt.% H_2O (Del Carlo & Pompilio, 2004; Métrich *et al.*, 2004; Corsaro & Pompilio, 2004a, 2004b; Spilliaert *et al.*, 2006; Moretti *et al.*, 2018; Zuccarello *et al.*, 2021, 2022) with H_2O up to 6 wt.% found more recently in the ~4-ka fall-stratified tephra (Gennaro *et al.*, 2019).

There are multiple well-documented zones of crystallization in the crust beneath Etna spanning from just below the edifice (~1–2 km) to near the crust–mantle boundary (~20–24 km) (Sharp *et al.*, 1980; Trigila *et al.*, 1990; Murru *et al.*, 1999; Chiarabba *et al.*, 2000; Armienti *et al.*, 2004, 2007; Nelson, 2015; Giuffrida & Viccaro, 2017; Ubide & Kamber, 2018; Giuffrida *et al.*, 2023). Furthermore, the ratio of plagioclase to mafic minerals (plagioclase/[clinopyroxene + olivine + Ti-magnetite]) for Etna's historical magmas is often >1, which suggests shallow crystallization is predominant (Métrich & Rutherford, 1998; Métrich *et al.*, 2004; Corsaro *et al.*, 2013).

GEOCHEMICAL AND MINERALOGICAL DATA UTILIZED IN STUDY

To evaluate the feasibility of the computational models, each model is compared to analytical data for 538 whole-rock samples and glass compiled from 18 studies spanning Etna eruptions from 1329 to 2005 CE. For analytical details of these studies refer to the original papers in Electronic Appendix 1. This study focuses on eight major oxides (SiO_2, TiO_2, FeO* [= FeO + Fe_2O_3 * 0.8998], Al_2O_3, MgO, CaO, Na_2O, and K_2O), five trace elements (Rb, Sr, Ba, La, Nd), and $^{87}Sr/^{86}Sr$. Other than Rb, which undergoes post-1971 enrichment, trace elements that do not undergo enrichment but are otherwise well-characterized at Etna were selected to cover a range of partitioning behaviors. Note that $^{87}Sr/^{86}Sr$ is not the only isotopic ratio to experience a shift in the post-1971 geochemical signature. There are corresponding decreases in whole-rock Nd–Pb–Hf isotopes (e.g. Viccaro *et al.*, 2011; Correale *et al.*, 2014). Sr isotopes are targeted for modeling here because they are extensively characterized in whole-rock samples and select crystal phases (Joron & Treuil, 1984; Armienti *et al.*, 1989, 2007; Barbieri *et al.*, 1993; Condomines *et al.*, 1995; Tonarini *et al.*, 1995). In this document, all observed major element oxides are reported in wt.% and trace elements in ppm (equivalent to μg/g).

Observed mineral proportions of ubiquitous phases are taken from a 1977 to 2005 sample subset (Electronic Appendix 2), which are consistent with limited reports of proportions for older eruptions in the studied period. The average observed phase assemblage is dominated by plagioclase feldspar (63%), followed by clinopyroxene (30%), olivine (7%), and Ti-magnetite (<1%).

THERMODYNAMIC MODEL AND PARAMETERS

Magma Chamber Simulator

The Magma Chamber Simulator (MCS) (Bohrson *et al.*, 2014, 2020; Heinonen *et al.*, 2020) is a thermodynamic model that represents the integration of MELTS (Ghiorso & Sack, 1995; Asimow & Ghiorso, 1998; Ghiorso *et al.*, 2002; Gualda *et al.*, 2012; Ghiorso & Gualda, 2015) and the energy- and mass-constrained theory of open magmatic systems developed in Spera & Bohrson (2001). MCS quantifies the chemical evolution (major and trace elements, isotopes, phase equilibria) of a magma body affected by concurrent and/or serial recharge *via* magma mixing (R), mush entrainment (E), crustal assimilation *via* partial melting (A) or stoping (S), and fractional crystallization (FC). Stoping is used to simulate the physical process by which wallrock is fractured and incorporated *en masse* into pre-existing magma. Stoped mass is thermodynamically treated the same as recharge magma or entrained mush (Bohrson *et al.*, 2014, 2020), and we simplify phrasing to only include stoped wallrock in the explanation below.

There are four subsystems (resident melt + cumulates [crystals formed during fractional crystallization] + wallrock ± stoped wallrock) for which initial model parameters are defined. A run begins with 100 mass units (m.u.) of resident magma at its liquidus temperature and with a user-defined composition and cooling increment (e.g. 5 °C). Also required are compositions, masses, and temperatures of the assimilated and stoped wallrock, as well as a critical melt fraction of wallrock (Fmzero in MCS), which represents a percolation threshold for anatectic melt mobility (typical values for crustal magmatic systems are 0.04 to >0.12; Bohrson *et al.*, 2020; see Bohrson *et al.*, 2014 for assumptions related to percolation threshold in MCS). Wallrock is modeled in isotopic equilibrium (i.e. all wallrock phases have identical $^{87}Sr/^{86}Sr$). When models are run with unconstrained fO_2, initial Fe_2O_3 and FeO compositions for each subsystem at a given pressure and temperature are defined using rhyolite-MELTS along a specified buffer and thereafter the fugacity of the oxygen is buffered by the ferrous/ferric Fe ratio of the melt. All masses reported here are either in m.u. (e.g. 5 m.u. of olivine formed in the resident melt) or percent, using the initial mass of magma as the comparison (e.g. 5% olivine formed); in MCS all masses are relative and can be scaled to any absolute amount.

An S_nAFC ($n \leq 30$) simulation proceeds as follows: (1) The resident magma, initially at its liquidus, cools and fractionally crystallizes; crystal phases are removed at each temperature decrement into a cumulate reservoir. The cumulate crystals are chemically isolated from but remain in thermal equilibrium with resident melt as cooling and crystallization proceeds. Sensible and latent heat from magma cooling and concomitant crystallization is transferred to wallrock, which heats up and may begin to melt.

(2) If the percolation threshold for the wallrock is surpassed, all partial melt produced over this critical value is instantaneously removed and added to the resident melt. (3) Stoped wallrock defined by its unique state (composition, mass, and temperature) is added to the magma body *via* bulk addition at any chosen resident melt temperature step. Upon stoping, the resident melt and newly added mass homogenize and thermodynamically re-equilibrate. Each simulation concludes when the magma body and wallrock are in thermal equilibrium or when a user specified temperature is reached (Bohrson *et al.*, 2014). Each step in the initial stage of the simulation utilizes mass and energy balance and thermodynamic constraints to provide major elements, masses, and temperatures for magma melt ± fluid phase, associated crystals, and residual wallrock, as well as the state of the stoped block at the instant before stoping. After solving for solid phases and major element compositions, MCS can calculate trace elements and isotopes with input of user-defined initial concentrations, isotopic ratios, and relevant partition coefficients (Heinonen *et al.*, 2020). Output includes trace element concentrations and isotope ratios for all parts of MCS subsystems.

Here, MCS modeling was originally broken into two steps (Fig. 3). Step one modeled pre-1971 data with the goal of defining a primitive parent magma composition to represent an uncontaminated starting material as well as its storage location and intensive parameters. Step two modeled post-1971 data with the goal of examining possibilities of crustal contamination of the parental magma through wallrock assimilation and stoping. Lastly, alternative parental magmas were re-examined due to unsatisfactory model fit of Na_2O and TiO_2 versus MgO. Modeling in all steps included sensitivity testing to identify parameters that exerted the most control on model outcomes. Best-fit MCS models were determined by phase equilibria comparison and visual inspection of modeled trends with the goals of capturing the main observed data trends and/or 'bracketing' the observed data (i.e. capturing the lower and upper limits of these data). Best-fit FC, AFC, SFC, and SAFC model inputs and outputs are available electronically and they include the trace element partition coefficients used. Since Etnean magmas typically erupt between 1000 °C and 1100 °C (e.g. Corsaro & Miraglia, 2005), models stop when the resident magma cools below 1000 °C. The magma cooling increment in models shown here is 5 °C. Model runs included in figures in this paper are intended to highlight the most distinguishing trends used to assess model fit. To examine any models that are referenced but not plotted here, see Supplementary Figs. 1–14 in Electronic Appendix 3. Finally, modifications made to initial compositions (e.g. changes to initial H_2O content) are summarized in Electronic Appendix 4.

Choice of parent magma and initial conditions

To choose a parent magma, we initially consider samples from sources outlined in Electronic Appendix 1 encompassing eruptions since 1329 (Fig. 2). Magmas with MgO <8 wt.% dominate this sample suite, and thus may have experienced crustal assimilation as they differentiated and are rejected. Another possible parent magma comes from Etna's ~4-ka fall-stratified tephra deposit (FS tephra; Kamenetsky *et al.*, 2007). This tephra contains euhedral crystals of olivine (<8% modal abundance; $Fo_{90–91}$), clinopyroxene (<3%; Mg# 96–92.5), and Cr spinel (<0.1%). The combination of mineral identities and compositions including high whole-rock MgO (12–17 wt.%), Ni (135–285 ppm), and Cr (920–1330 ppm) concentrations are interpreted by Kamenetsky *et al.* (2007) to represent a primitive, unfractionated magma that may be the parent for more recent eruptive products. An FS tephra sample is thus used as a proxy for a parent magma (PM) composition for pre- and post-1971 Etnean lavas (Tables 1 and 2).

Via fractional crystallization, variations in pressure, initial H_2O content, and initial fO_2 of PM are examined to determine the best-fit initial conditions of the parent magma ($n \approx 75$ models); these conditions are then utilized as the starting point for assimilation and stoping models. A summary of the range of parameters tested in PM FC modeling is listed in Table 3. Saturation of plagioclase in these models is a key determining factor in choosing initial conditions. Plagioclase phenocrysts in both historic to recent activity are sizeable (1–5 mm, sometimes ≤10 mm) and have complex growth patterns (e.g. Viccaro *et al.*, 2010, 2016). It is unlikely, then, that these phenocrysts grew exclusively late and upon ascent. Modeled initial H_2O >1.0 wt.% delays the onset of plagioclase crystallization and thus yields a poor model fit for whole-rock Al_2O_3 versus MgO (Supplementary Fig. 1). Figure 4 shows models of PM with 1 and 4 wt.% initial H_2O fractionally crystallizing at 0.2 and 0.5 GPa. Plagioclase crystallization is suppressed completely during FC of PM with 4 wt.% initial H_2O at 0.5 GPa, and only 1.7 m.u. crystallizes in the final 10 °C of cooling at 0.2 GPa (Fig. 4b). Although $H_2O \leq 6$ wt.% is recorded in the FS tephra (Gennaro *et al.*, 2019), plagioclase behavior suggests that high magma water contents are unlikely to be the prevailing conditions leading to generation of historical to recent Etnean magmas. High H_2O contents observed in olivine- and clinopyroxene-hosted melt inclusions in historical and recent lavas can, therefore, be explained assuming complex dynamics of degassing and/or flushing of volatiles (H_2O-CO_2) occurring in the range of 0.2 to 0.4 GPa (e.g. Métrich *et al.*, 2004; Spilliaert *et al.*, 2006; Ferlito *et al.*, 2008; Gennaro *et al.*, 2019; Zuccarello *et al.*, 2021, 2022), together with H_2O acting incompatibly during crystallization. In this regard, at 0.2 GPa pressure, fractional crystallization of the model PM yielded derivatives with MgO of 1 to 8 wt.% and H_2O from 1.6 to 5.0 wt.%. In addition, primary magmas with initial H_2O of 0.5 wt.% are unlikely, as volatile-poor (<1.0 wt.% $H_2O + CO_2$) Etnean magmas would likely stall at ~22 km deep in the crust from insufficient buoyancy relative to basement rocks (Corsaro & Pompilio, 2004c). Therefore, a parent magma with ~1.0 wt.% initial H_2O is a reasonable starting composition based on model results and literature constraints. Crystallization of PM with 1.0 wt.% initial H_2O at 0.5 GPa also suppresses plagioclase crystallization with just 1.6 m.u. forming in the final 45 °C of cooling (Fig. 4b), and pressures exceeding 0.5 GPa produce exceptionally poor model fits relative to observed whole rock SiO_2, Al_2O_3, and FeO* versus MgO (Supplementary Fig. 2). Thus, to produce a phase assemblage consistent with observations, we eliminate pressures >0.2 GPa. Pressures of 0.2 and 0.1 GPa are virtually indistinguishable for TiO_2, FeO*, Na_2O, and K_2O and similar for SiO_2 and CaO versus MgO. Plagioclase saturates earlier during FC at 0.1 GPa, and the model reaches only the lowest values of Al_2O_3. Therefore, a pressure of 0.2 GPa (~6 km depth) is preferred as the best-fit, which is in agreement with studies that place at least part of the major crystallization zone in the upper-middle crust within the sedimentary basement (2–15 km depth; Loddo *et al.*, 1989; Yellin-Dror *et al.*, 1997; Tibaldi & Groppelli, 2002; Bousquet & Lanzafame, 2004; Corsaro & Pompilio, 2004b). Interaction between the magma's transport and storage system and the sedimentary basement is further supported by sedimentary and metamorphic xenoliths recovered from Etnean lavas (e.g. Michaud, 1995; Lanzafame *et al.*, 2003; Corsaro *et al.*, 2007; Coulson *et al.*, 2011).

Changes in the initial ferric and ferrous iron content are determined under oxygen buffers from QFM-2 to QFM + 2 *via* rhyolite-MELTS version 1.2.0; using these initial fO_2 conditions, the models

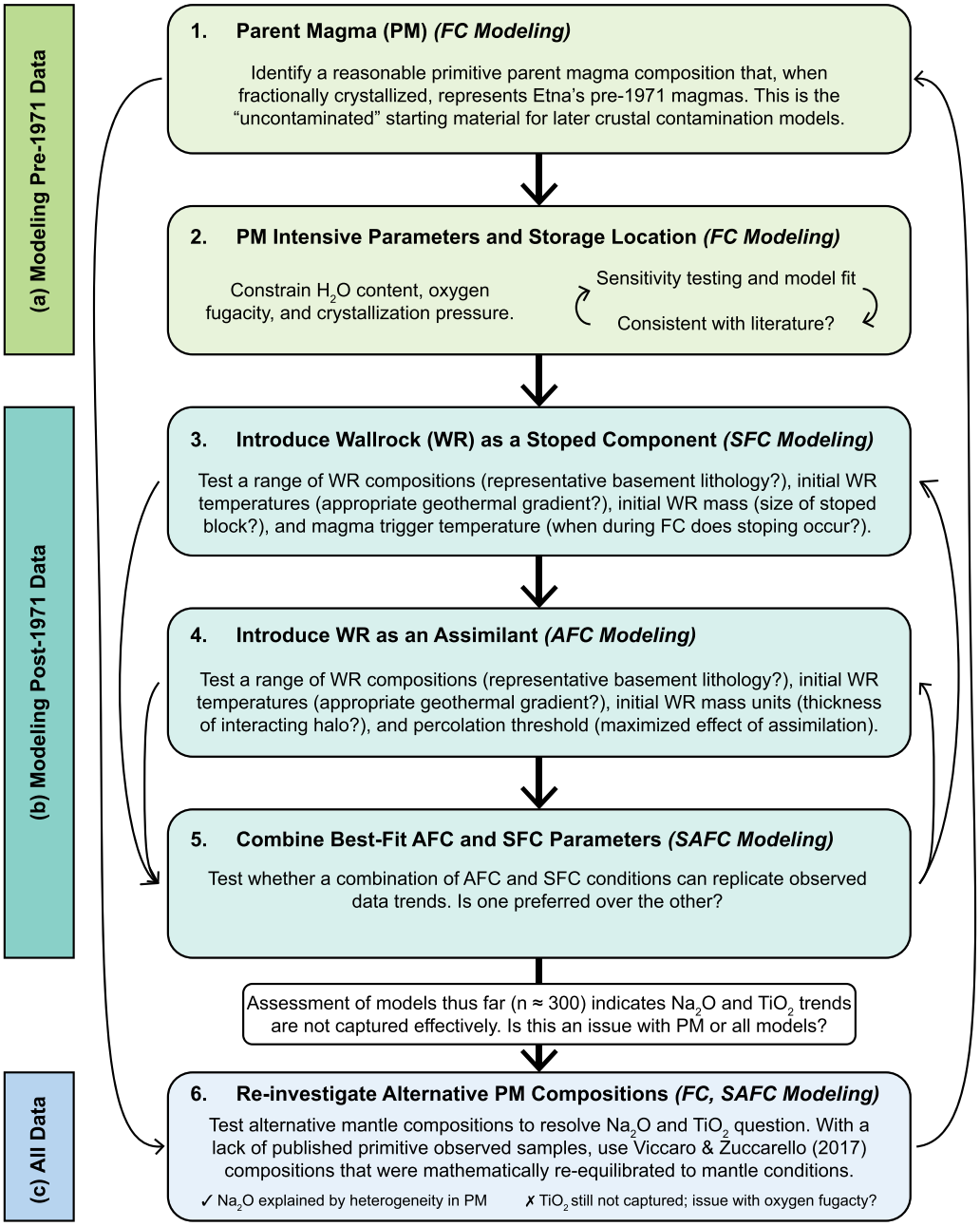

Fig. 3. Flowchart illustrating a general roadmap of the MCS modeling process, which was initially broken into two steps with goals of modeling (**a**) pre-1971 data and (**b**) post-1971 data. Due to undesirable fit of Na_2O and TiO_2 (wt.%) in all models, (**c**) alternative PM compositions were re-investigated.

are run unconstrained (i.e. no oxygen buffer was used). This range of fO_2 produced models with different TiO_2 and FeO∗ in the evolving melt but has negligible effects on all other oxides (Supplementary Fig. 3). Variations in this parameter does capture different ranges of whole-rock FeO∗ values, suggesting the oxygen fugacity has varied through time. We use QFM as the fO_2 for all remaining models, which is reasonable for Etnean lavas (Kahl *et al.*, 2015, 2017).

In summary, best-fit results for the FC model trend of PM include an initial H_2O content of 1.0 wt.%, pressure of 0.2 GPa, and initial ferric and ferrous iron composition determined by an oxygen buffer of QFM (Fig. 4). FC of PM under these conditions yields olivine, clinopyroxene, plagioclase, and minor spinel and apatite, which is in excellent agreement with the dominant observed phase assemblage. Notably, PM's K_2O-MgO evolution successfully captures the pre-1971 whole-rock trend as opposed to the enriched post-1971 trend. Fractionation of PM effectively captures the middle range of the observed data when SiO_2 and CaO are plotted versus MgO, and the upper range of FeO∗ and its glass compositions, while it is consistently low in Na_2O and TiO_2 vs MgO. The slope of the model's MgO-Al_2O_3 evolution aligns with the observed data but does not reach the upper range from approximately 17 to 20 wt % Al_2O_3 at <6 wt.% MgO.

The initial parental magma $^{87}Sr/^{86}Sr$ is estimated based on the least radiogenic sample in the data compilation (~0.7033) and is not addressed further because this value does not vary in FC models. Initial concentrations of Rb, Sr, Ba, La, and Nd are estimated based on the range of values from the ~4-ka FS tephra analyzed by Kamenetsky *et al.* (2007). This FC trace element model (Fig. 5h-m) captures the pre-1971 Rb trend exceptionally well, and

Table 1: Initial magma and wallrock compositions utilized in MCS models reported by wt.%

	SiO_2	TiO_2	Al_2O_3	Fe_2O_3	FeO	MnO	MgO	CaO	Na_2O	K_2O	P_2O_5	H_2O	CO_2
Initial Resident (Parent) Magma Compositions													
PM[a]	47.13	0.85	9.99	1.51	7.87	0.17	16.93	12.22	1.31	0.61	0.22	0.99	0.20
ET75[b]	45.41	1.43	14.76	1.76	9.14	0.20	11.61	10.51	2.20	1.08	-	1.91	-
Pre-1971[b]	45.12	1.66	14.78	1.74	9.14	0.17	11.42	9.93	2.88	0.99	-	2.19	-
Post-1971[b]	44.99	1.73	14.75	1.75	9.05	0.17	10.92	10.30	2.68	1.34	-	2.34	-
Initial Wallrock Compositions													
Flysch[c]	69.69	0.62	14.13	2.98	1.07	0.05	1.71	1.46	2.41	2.95	-	1.78	1.15
Skarn 1[d]	45.23	0.36	13.42	2.69	0.81	0.06	13.76	21.44	0.36	1.84	0.03	-	-
Skarn 2[d]	52.61	0.08	0.55	0.67	0.26	0.04	18.41	26.92	0.28	0.07	0.10	-	-
Skarn 3[e]	37.26	0.97	20.42	5.14	1.27	0.11	13.03	21.70	0.02	0.00	0.08	-	-
90:10[f]	67.24	0.60	14.06	2.95	1.04	0.05	2.91	3.45	2.20	2.84	0.00	1.60	1.04
80:20	64.79	0.57	13.99	2.92	1.02	0.05	4.12	5.45	2.00	2.73	0.01	1.42	0.92
70:30	62.35	0.54	13.92	2.89	0.99	0.05	5.32	7.45	1.79	2.62	0.01	1.24	0.81
60:40	59.90	0.52	13.85	2.86	0.97	0.05	6.53	9.45	1.59	2.51	0.01	1.07	0.69
50:50	57.46	0.49	13.77	2.83	0.94	0.06	7.74	11.45	1.38	2.40	0.02	0.89	0.58
40:60	55.01	0.46	13.70	2.81	0.92	0.06	8.94	13.45	1.18	2.28	0.02	0.71	0.46
30:70 (Mixture 1)	52.57	0.44	13.63	2.78	0.89	0.06	10.15	15.45	0.97	2.17	0.02	0.53	0.35
20:80	50.12	0.41	13.56	2.75	0.86	0.06	11.35	17.45	0.77	2.06	0.02	0.36	0.23
10:90	47.68	0.38	13.49	2.72	0.84	0.06	12.56	19.44	0.56	1.95	0.03	0.18	0.12

See Electronic Appendix 4 for modifications made to original compositions. [a]Original composition modified from sample svp291-D of Kamenetsky *et al.* (2007). [b]Original compositions taken from Viccaro & Zuccarello (2017). [c]Original composition taken from Clocchiatti *et al.* (1988). [d]Original compositions taken from Di Rocco *et al.* (2012). [e]Original composition taken from Jolis *et al.* (2015). [f]Ratios represent wallrock mixtures with varying proportions of Flysch to Skarn 1 (e.g. 90:10 = 90 parts Flysch to 10 parts Skarn 1).

Table 2: Measured and estimated trace element concentrations (reported by ppm) and Sr isotopes used in MCS models

	Rb	Sr	Ba	La	Nd	$^{87}Sr/^{86}Sr$
PM[a]	14.5	506	240	18.9	18.9	0.7033
Flysch[b]	49	879	400	40	15	0.71776
Skarn 1[c]	121	350	1338	20	30	0.7075
Skarn 2[c]	121	350	1338	20	30	0.7075
Skarn 3[c]	121	350	1338	20	30	0.7075
90:10	56	826	494	38	17	0.7173
80:20	64	773	588	36	18	0.7168
70:30	71	720	681	34	20	0.7163
60:40	78	667	775	32	21	0.7156
50:50	85	615	869	30	23	0.7148
40:60	92	562	963	28	24	0.7139
30:70 (Mixture 1)	99	509	1057	26	26	0.7128

[a]Trace element concentrations taken from the ~4-ka tephra sample set of Kamenetsky *et al.* (2007); Sr isotope ratio is estimated from the least radiogenic sample in the data compilation provided in Electronic Appendix 1. [b]Trace element concentrations taken from Mikes *et al.* (2006); Sr isotope ratio taken from Armienti *et al.* (1989). [c]Rb and Ba concentrations from Jolis *et al.* (2015); Sr, La, and Nd concentrations estimated based on a range of skarn compositions from Del Moro *et al.* (2001); Sr isotope ratios estimated based on age of the carbonate Hyblean Plateau (Yellin-Dror *et al.*, 1997) from the Sr seawater curve of McArthur *et al.* (2001). Ratios represent wallrock mixtures with varying proportions of Flysch to Skarn 1 (e.g. 90:10 = 90 parts Flysch to 10 parts Skarn 1).

Table 3: Summary of parameters tested in fractional crystallization modeling for PM

	Range of Parameters
Pressure (GPa)	0.1, 0.2, 0.5, 0.8, 1.1
Initial H_2O content (wt %)	0.5, 1.0, 2.0, 3.0, 4.0, 5.0
Initial fO_2	QFM-2, QFM-1, QFM, QFM + 1, QFM + 2

it also captures either the lower limits or the middle trend of Ba, Sr, La, and Nd. These elements (except for Sr) increase in concentration with decreasing MgO. Sr initially behaves incompatibly but changes to compatible behavior at ~6 wt.% MgO, which is where plagioclase saturates during FC. This trend is consistent with the compatibility of Sr in plagioclase.

Crustal contamination models

To evaluate the role of crust-magma interaction on post-1971 magmas, we begin with the defined parent magma and initial conditions outlined above; the use of a ~4-ka magma as the parent assumes that the parent magma has broadly remained the same for the last several thousand years (Kamenetsky *et al.*, 2007). To document specific consequences of assimilation versus stoping on the parent magma, a subset of AFC-only and SFC-only runs are presented, followed by combined SAFC models. Subsequently, trace elements are calculated for the best-fit major element models to define the final best-fit model(s) based on major elements, phase equilibria, trace elements, and Sr isotopes.

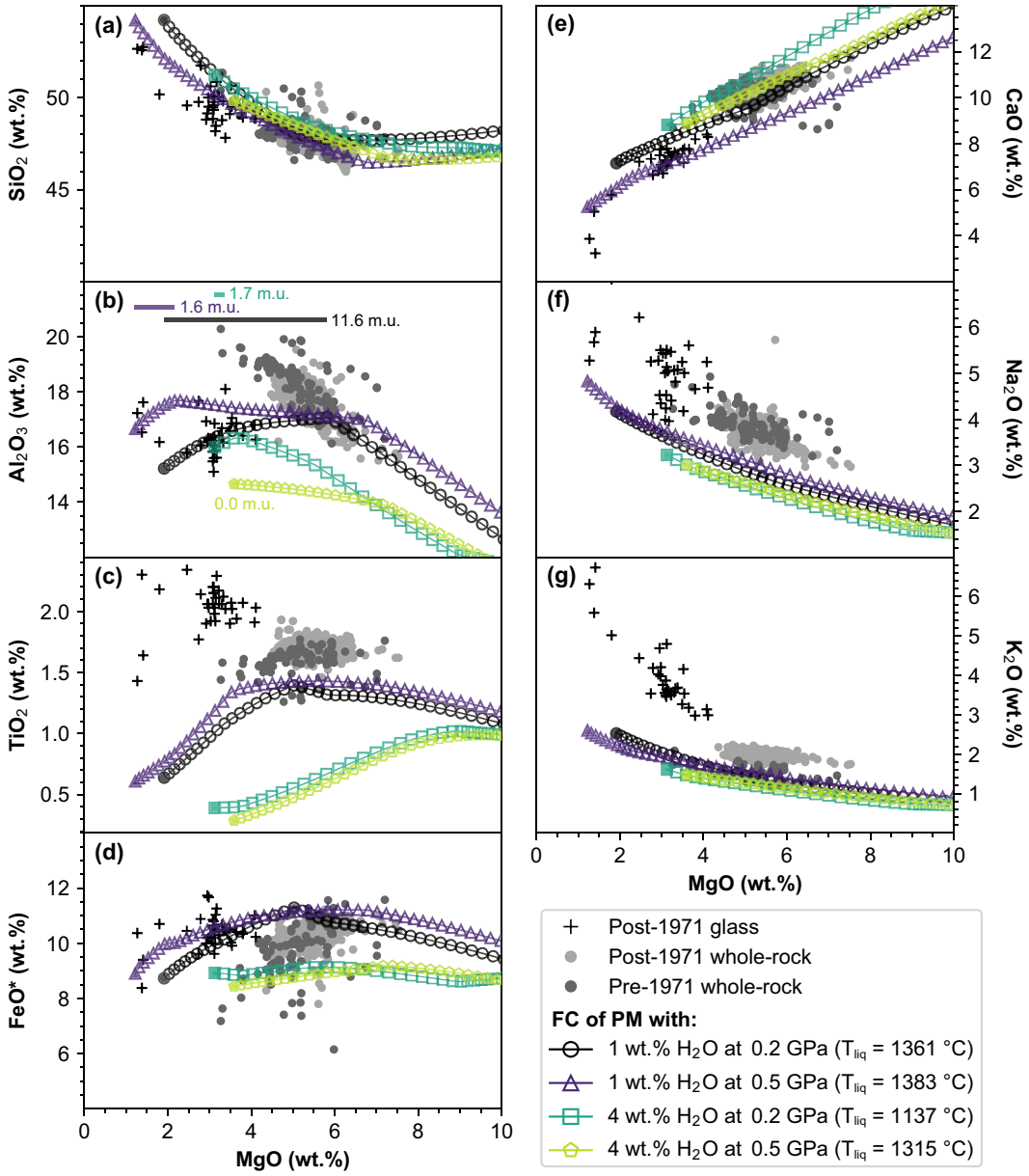

Fig. 4. MCS major element FC trends of model PM with 1 and 4 wt.% initial H_2O, both run at pressures of 0.2 and 0.5 GPa, compared to observed data for MgO (wt.%) versus (**a**) SiO_2, (**b**) Al_2O_3, (**c**) FeO∗, (**d**) TiO_2, (**e**) CaO, (**f**) Na_2O, and (**g**) K_2O (wt.%).The liquidus temperature (T_{liq}) of each starting magma is indicated in the legend. Models progress from right to left and the last step of the model (T = 1000 °C) is denoted by a filled symbol. Bold lines in **(b)** indicate the model interval over which plagioclase saturates including its total crystallized mass in m.u. Refer to Table 1 for initial magma compositions.

As illustrated above, FC alone cannot account for the full range of data evidenced in Etnean lavas, particularly for post-1971 K_2O, Rb, and $^{87}Sr/^{86}Sr$ versus MgO. Heterogeneous Sr isotopes require crustal contamination and/or mantle heterogeneity manifested through recharge of heterogeneous melts. Contamination *via* assimilation and stoping are well-documented in the literature as effective mechanisms for contaminating magmas (e.g. Furlong & Myers, 1985; Del Moro *et al.*, 2001; Chadwick *et al.*, 2007; Erdmann *et al.*, 2010; Borisova *et al.*, 2013). Carbonate, calc-silicate, aluminosilicate, and composite xenoliths documented in Etnean lavas (e.g. Michaud, 1995) provide evidence that stoped and/or assimilated wallrock may play a role in the alkali enrichment. Although sedimentary xenoliths have been recovered in Etnean magmas, no existing studies analyze their whole-rock compositions. Because of this, the Capo d'Orlando flysch, which has been suggested as a source of crustal contamination in Etnean lavas (Clocchiatti *et al.*, 1988; Armienti *et al.*, 1989; Marty *et al.*, 1994), is used to represent the sediments in the uppermost 2 to 5 km beneath the volcanic pile (Flysch; Tables 1 and 2). To represent the carbonate-dominated Hyblean Plateau, we attempted to use limestone and dolomite compositions as the wallrock. However, no successful AFC models with carbonate-only wallrock were produced. Nonetheless, the interaction between carbonate rocks and heat supplied by magmatic activity can induce physical, chemical, and mineralogical changes (i.e. contact metamorphism). Due to the thermal alteration evident in Etnean carbonate xenoliths such as those documented by Michaud (1995), along with the long-lived (~500 kyr) magmatic activity at Etna, we assume that some carbonate rocks in contact with Etna's magma storage system were metamorphosed into magmatic skarns. A variety of skarn

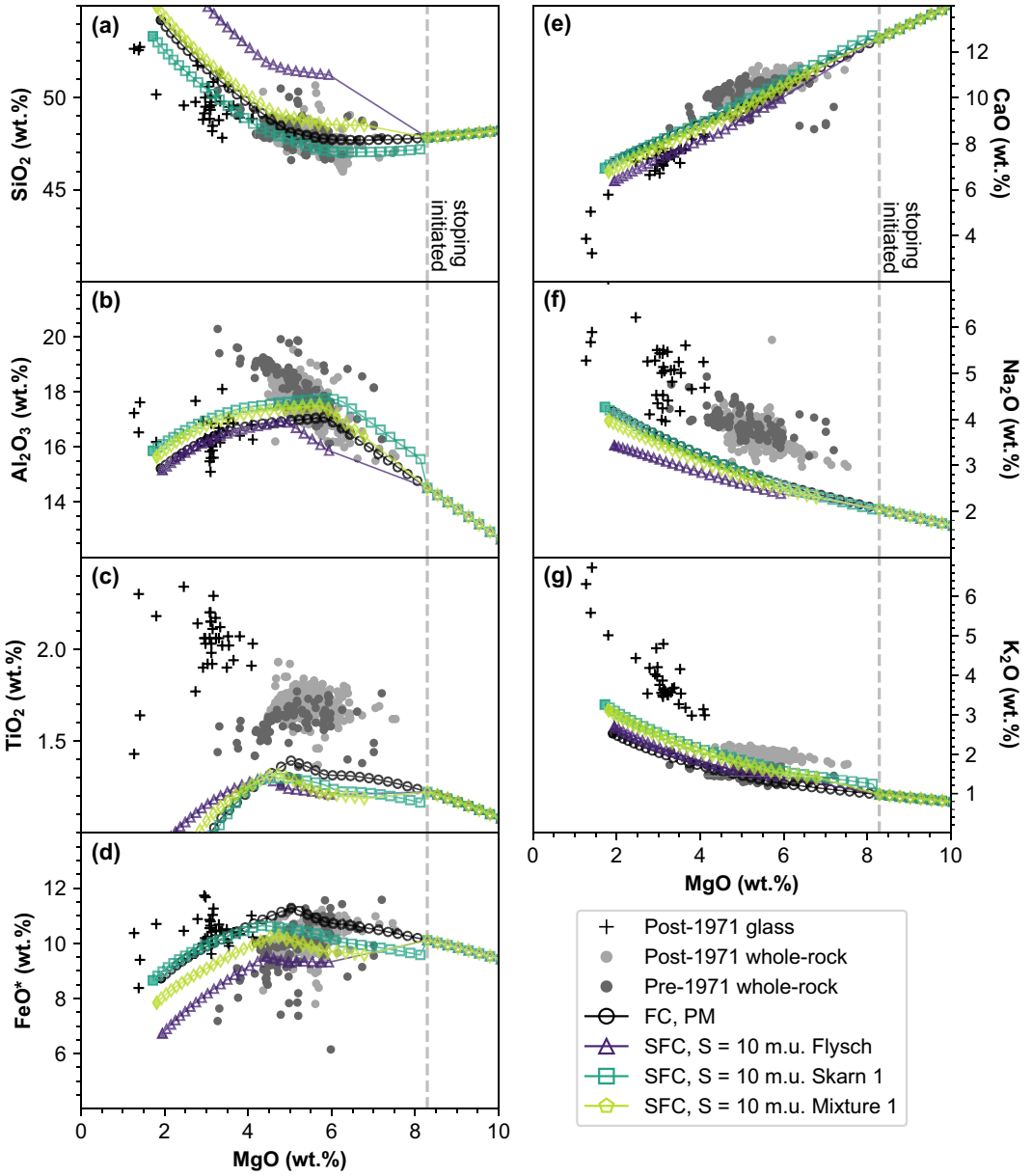

Fig. 5. Modeled SFC trends produced *via* stoping 10 m.u. of Flysch, Skarn 1, and Mixture 1 compared to observed data, plotted as MgO (wt.%) versus (**a**), SiO_2, (**b**) Al_2O_3, (**c**) TiO_2, (**d**) FeO*, (**e**) CaO, (**f**) Na_2O, (**g**) K_2O (wt.%), (**h**) Rb, (**i**) Sr, (**j**) Ba, (**k**) La, (**l**) Nd (ppm), and (**m**) $^{87}Sr/^{86}Sr$. FC trend of the model PM is shown for comparison to a modeled magma unaffected by crustal contamination. Dashed gray line indicates the FC step after which stoping is triggered. Model progression is as described in Fig. 4. Refer to Tables 1 and 2 for initial magma and wallrock compositions.

xenoliths from the Italian regions of Vesuvius (Jolis *et al.*, 2015) and Colli Albani (Di Rocco *et al.*, 2012) are used as proxies for Etna's carbonate substrata. Finally, to reflect heterogenous stratigraphy (e.g. interbedded layers of sandy shale and limestone), mixtures of the Capo d'Orlando flysch and Skarn 1 in 10% increments are also tested as potential wallrock compositions (Tables 1 and 2).

MCS stoping and fractional crystallization (SFC) modeling results

Approximately 70 SFC models are examined in this study. For SFC models, additional user-defined variables include the bulk composition, mass, and temperature of the stoped wallrock, and the resident magma body temperature at which the block is stoped (i.e. in MCS, the magma trigger temperature) (tested ranges listed in Table 4). Based on results of models with initial stoped block temperatures of 750 °C to 1250 °C, model sensitivity to the stoped block temperature is negligible (examples of Skarn 1 at 1165 and 1250 °C shown in Supplementary Fig. 4), and thus the stoped block temperature is set near a given composition's solidus temperature (706–1193 °C). Likewise, assessment of models illustrates variations from 950 °C to 1200 °C in the magma trigger temperature does not affect the overall parental magma's compositional evolution significantly. For example, evolutionary trends using trigger temperatures of 1095, 1130, and 1165 °C, which are chosen to initiate stoping at various points along the MgO interval of observed data, are nearly indistinguishable except in TiO_2 vs. MgO (Supplementary Fig. 5). Therefore, stoping is triggered in most models at a magma temperature of 1165 °C to capture trends of observed samples with the highest MgO.

About 55 models are run to assess the impact of stoped block composition and masses on model outcomes. In the remainder

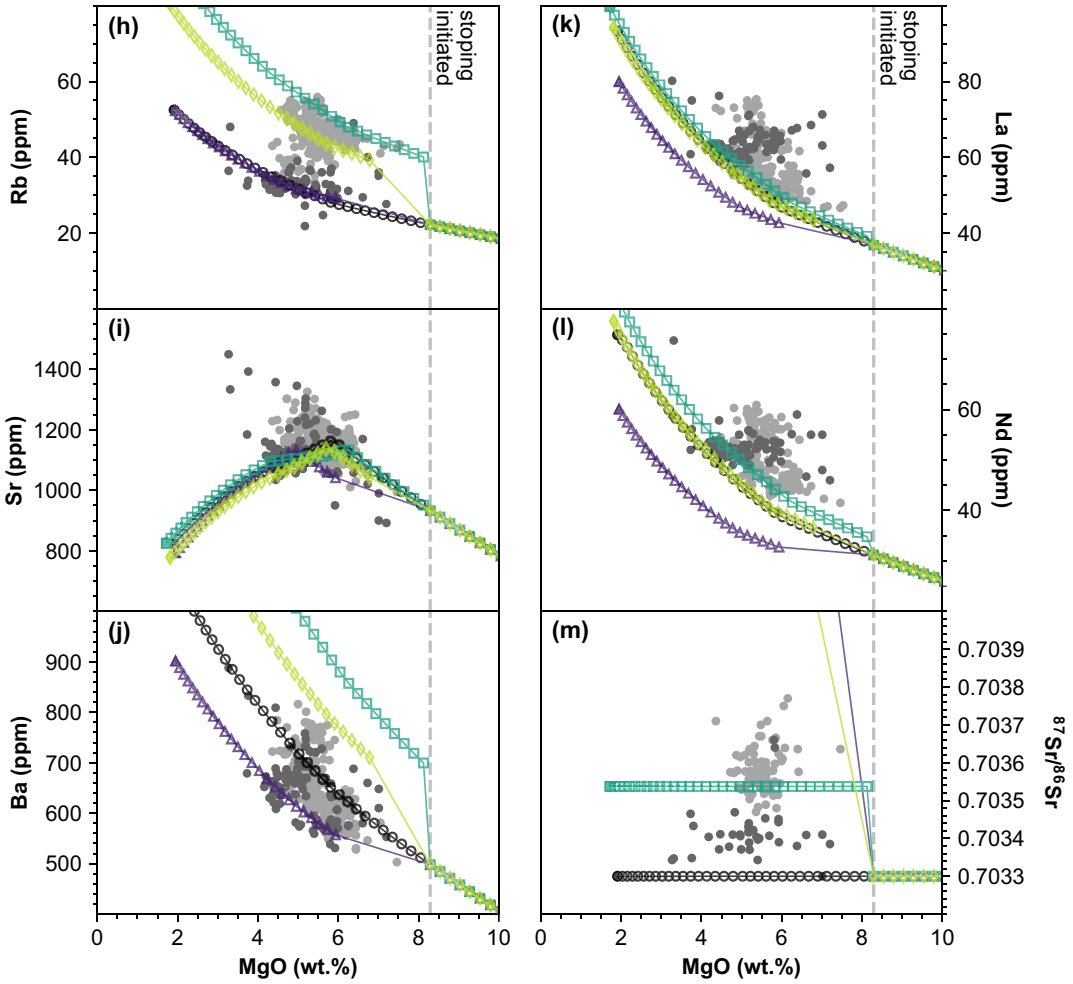

Fig. 5. Continued.

Table 4: Summary of parameters tested in crustal contamination models

	AFC	SFC	SAFC
Number of Runs[a]	65	70	40
WR[b] Compositions Tested	11	-	6
WR Initial Mass Units (m.u.)[c]	25–100	-	75–100
WR Initial T (°C)	200–500	-	200
Fmzero	0.02–0.12	-	0.05
S[b] Compositions Tested	-	8	6
S Mass Units	-	2–80	2–60
S Initial T (°C)	-	750–1250	750–1250
S Trigger T (°C)	-	950–1200	1140–1185

[a]These runs were performed with PM as the initial composition with the best fit FC parameters outlined in the text. [b]WR, wallrock; S, stoped block [c]WR initial mass is set relative to the magma body mass, which is always 100 m.u.

of this section we refer to Figure 5, which shows model results of stoping 10-m.u. blocks of Capo d'Orlando Flysch, Skarn 1, and Mixture 1 for illustrative purposes. Model results from stoping additional skarn compositions (Skarns 1, 2, and 3; Supplementary Fig. 6) and masses (2, 5, 10, and 20 m.u.) for Capo d'Orlando Flysch, Skarn 1, and Mixture 1 (Supplementary Figs. 7–9, respectively) are found in Electronic Appendix 3. Amounts of 2 to 20 m.u. of stoped Capo d'Orlando flysch produce substantial misfits for numerous trends (e.g. MgO versus SiO_2 and $^{87}Sr/^{86}Sr$), and stoping this material does not significantly increase the concentrations of K_2O or Rb in the derivative melts. The smallest tested amount of 2 m.u. is the only model that does not overestimate $^{87}Sr/^{86}Sr$. Flysch is, therefore, eliminated as a stoped contaminant. In addition, three different skarn compositions (Skarns 1, 2, and 3) and a skarn and flysch mixture (Mixture 1, 30:70 flysch:skarn) are stoped. Mixture 1 is the mixture utilized most in AFC models due to its agreeable solidus temperature and chemical composition as an assimilant (see Tables 1 and 2 and discussion in the following section on wallrock heterogeneity and solidi for further details). In general, the skarns and Mixture 1 are Ca- and Mg-rich relative to the resident magma composition at the instant of stoping (~8 wt.% MgO), and their addition results in increases in CaO

and MgO in the contaminated magma melt. Responses of the ~8 wt.% MgO melt with respect to the remaining oxides depend on the composition of a given stoped block. For example, upon stoping, Skarn 1 and Mixture 1 increase the melt K_2O, but Skarn 3 decreases it, and Skarn 3 increases Al_2O_3, whereas Skarn 2 decreases it. Furthermore, the modeled phase assemblages of olivine, clinopyroxene, plagioclase, and spinel ± apatite are still in excellent agreement with observed phase assemblages. Since Skarn 1 and Mixture 1 yield the necessary K_2O increase observed in post-1971 samples, these compositions are used to assess the sensitivity of model results to stoped mass.

Mass variations in stoped blocks (Skarn 1 and Mixture 1) for a given composition produce effects in the resident magma melt proportional to the mass (Supplementary Figs. 8–9). That is, larger stoped masses yield more drastic increases or decreases in affected oxides. Skarn 1 and Mixture 1 both induce changes to the derivative melts needed to capture observed post-1971 trends, including increases in K_2O, Rb, and $^{87}Sr/^{86}Sr$. However, large enough increases in K_2O are not possible without overestimating the Rb, Ba, and $^{87}Sr/^{86}Sr$ characteristics of the observed products. Models including 20 m.u. of stoped Skarn 1 and Mixture 1 capture post-1971 K_2O versus MgO, but the addition of Skarn 1 overestimates Rb and Ba, and the addition of Mixture 1 overestimates $^{87}Sr/^{86}Sr$. As a result, stoped masses are limited to rather small amounts. In these models, the derivative magmas generated *via* 2 m.u. of stoped Skarn 1 and Mixture 1 are selected as the best-fit model in the stoped mass and composition sensitivity tests because crystallizing phases are consistent with observations and these models capture the range of selected major oxides (except TiO_2 and Na_2O), trace elements, and $^{87}Sr/^{86}Sr$ without overestimating key geochemical parameters. However, minor additions of these wallrocks are insufficient to capture post-1971 K_2O, Rb, and $^{87}Sr/^{86}Sr$ trends, and thus stoping alone cannot explain the alkali enrichment.

MCS assimilation and fractional crystallization (AFC) modeling results

For AFC models (n ≈ 65), additional user-defined variables include the initial mass, temperature, and composition of the wallrock, as well as the percolation threshold (Fmzero) (Table 4). The percolation threshold was 0.05 for most runs, which falls within the typical range for crustal magmas (Bohrson *et al.*, 2020). Sensitivity tests demonstrate that a value of 0.05 initiates assimilation earlier than a value of 0.12; however, the overall evolution of the contaminated melts follow similar trajectories (Supplementary Fig. 10). Sensitivity of models to initial wallrock mass primarily changes the point at which assimilation begins, since larger masses require more enthalpy delivered from cooling and crystallization of magma to initiate partial melting in wallrock. The onset of assimilation due to these mass differences produces substantial differences in derivative melts (example masses of 40, 75, and 110 m.u. shown in Supplementary Fig. 11). The wallrock initial mass for most models is 100 m.u., which equates to a ~100-m-thick aureole for a hypothetical spherical magma body with a 1-km diameter (Heinonen *et al.*, 2019). Like initial mass, initial wallrock temperature controls the point at which contamination begins (examples of 50, 200, and 350 °C shown in Supplementary Fig. 12). At the chosen mass, the best-fit initial temperature of 450 °C represents wallrock that is thermally primed at approximately 3x that of a typical geotherm (25 °C/km). The initial composition of the wallrock (and its associated solidus) produces the most substantial model variability, and thus is the focus of the discussion below.

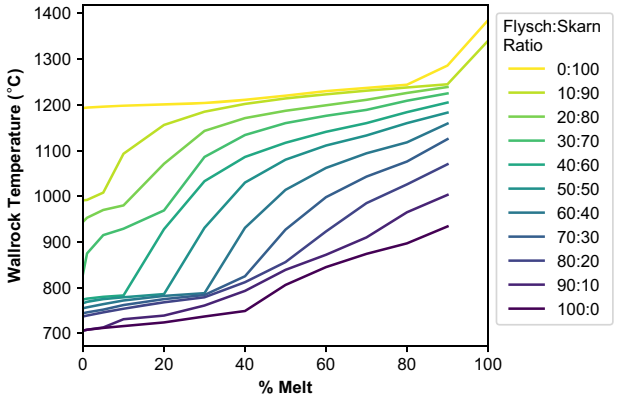

Fig. 6. The physical state of various wallrock compositions (plotted by mixing ratios of flysch:skarn) at temperatures from their solidus (0% melt) to liquidus (100% melt) determined by rhyolite-MELTS. Solutions for liquidi are not shown where rhyolite-MELTS did not converge on one. Note the broad range in wallrock solidi from flysch (100:0, 706 °C) to skarn (0:100, 1193 °C) and that the addition of just 10% of flysch to skarn (i.e. 10:90) lowers the wallrock solidus by over 200 °C.

A wallrock's composition affects its solidus, which in turn affects the efficiency with which anatectic melts are produced and thus the fertility of the wallrock to yield contaminated magmas. The Capo d'Orlando flysch has a solidus of 706 °C at 0.2 GPa determined by rhyolite-MELTS. In contrast, investigated skarns are relatively restitic and yield solidi temperatures up to 1193 °C (Figure 6). Because PM's liquidus is at 1361 °C, for typical geothermal gradients, the amount of enthalpy delivered by its fractionation is likely insufficient to produce substantial anatectic melt from skarns. This idea is confirmed by AFC models with skarn as the wallrock; magma-wallrock thermal equilibrium is consistently reached before skarn wallrock melts are produced over the range of observed MgO in Etnean lavas, and thus pure skarn is eliminated as a potential assimilant. Wallrock of flysch-skarn mixtures with ≥80% skarn behave in a similar manner and are also unlikely assimilants.

When skarn and flysch compositions are mixed in various proportions to represent a heterogenous and interbedded sedimentary basement, the solidi fall within the range defined by flysch and skarn endmembers. For example, when just 10% flysch is added to skarn, the solidus decreases >200 °C at 0.2 GPa according to rhyolite-MELTS (Fig. 6). Consequently, assimilation of the sedimentary basement may either involve a pure flysch or a flysch-skarn mixture with ≤70% of a skarn endmember. Initial phase assemblages of these wallrocks according to rhyolite-MELTS are plagioclase, K-feldspar, quartz, biotite, and orthopyroxene ± spinel, rhombohedral oxide, clinopyroxene, garnet, olivine, and sillimanite. Figure 7 illustrates select major oxide and trace element compositions of incremental anatectic melts produced from melting of flysch and 70:30, 50:50, and 30:70 flysch:skarn mixtures. Consistently over all AFC runs, quartz, biotite, and K-feldspar completely melt (Fig. 7a). During melting, compared to the initial wallrock composition, wallrock melts display increases in FeO* and Na_2O (7c,e). Wallrock melts of the 70:30 mixture and flysch are Si-rich (≤75 wt.% SiO_2), whereas wallrock melts of the 50:50 and 30:70 mixtures have melts with ~58 wt.% SiO_2 (Fig. 7b). In each wallrock, quartz is present and melts completely by the end of model runs, but the 70:30 mixture and flysch have significantly more quartz than the wallrock mixtures with more skarn, accounting for the Si-rich melts in the former. Melts of the

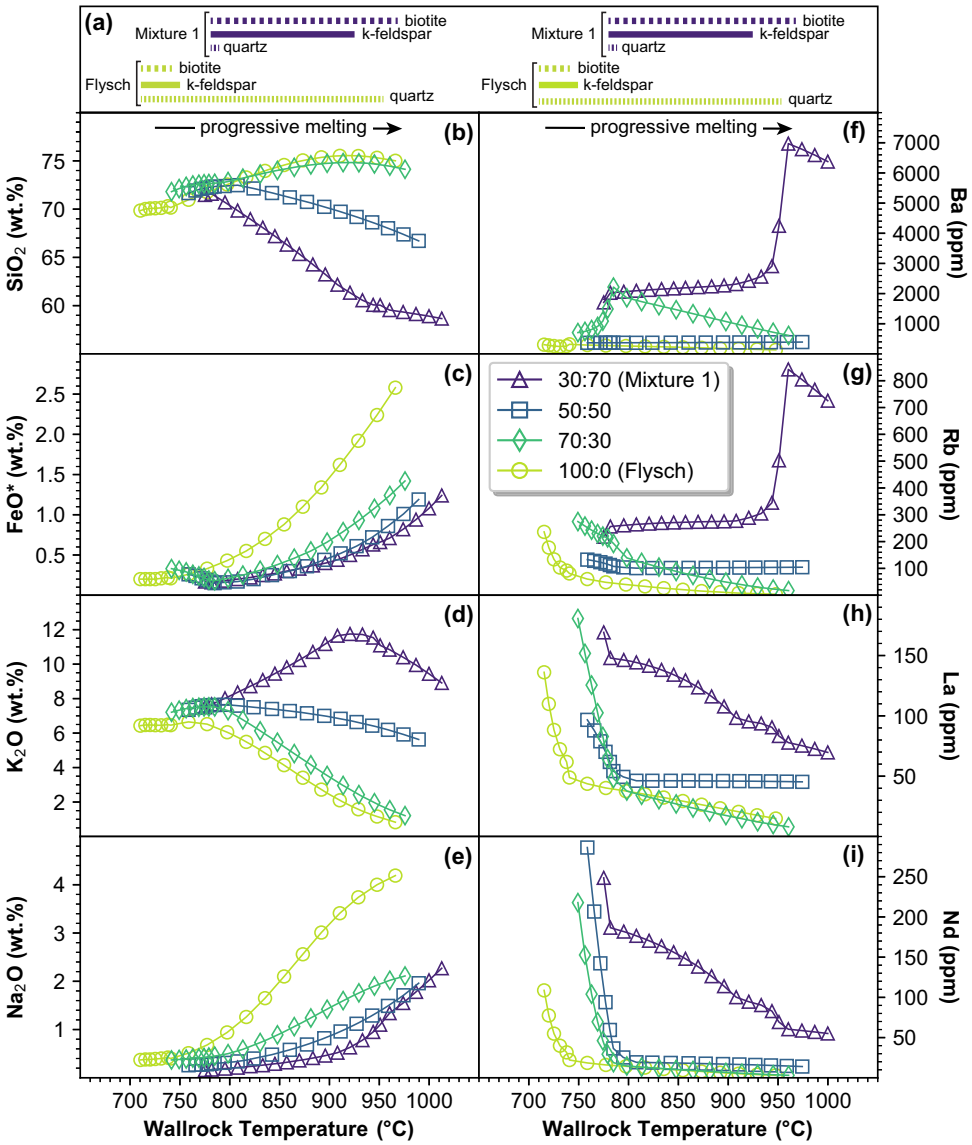

Fig. 7. Incremental partial melt compositions of wallrock produced as the wallrock increases in temperature during a given AFC run, with melting phases highlighted in (**a**), progressing from left to right and plotted as wallrock temperature (°C) versus wallrock partial melt (**b**) SiO_2, (**c**) FeO∗, (**d**) K_2O, (**e**) Na_2O (wt.%), (**f**) Ba, (**g**) Rb, (**h**) La, and (**i**) Nd (ppm). Bars at the top of the figure indicate the range over which different phases are present in the wallrock for the endmembers of Flysch and Mixture 1. Ratios listed represent the ratio of Flysch to Skarn 1 in a mixed composition. Initial wallrock compositions are given in Tables 1 and 2.

50:50 and 30:70 wallrock mixtures have the highest concentrations of K_2O (Fig. 7d). Again, this results from differences in the phase assemblages. The 50:50 and 30:70 mixtures are dominated by clinopyroxene, which does not melt, and plagioclase, which experiences limited melting. Consequently, the effects of melting K-rich biotite and K-feldspar are maximized. In comparison, the 70:30 mixture and flysch are dominated by quartz, which melt completely and dilute the compositional effects of other melted phases. All wallrock melts display initially high concentrations of La and Nd (Fig. 7h-i), owing to their incompatible nature in the melting assemblage, with their concentrations decreasing over the course of melting. Rb and Ba exhibit a range of behaviors in the wallrock melts (Fig. 7f-g). In these cases, we interpret the melting of biotite and possibly K-feldspar in the wallrocks as the major controls on concentrations of Rb and the melting of biotite and K-feldspar as the likely controls on the concentrations of Ba.

The remainder of this section references Fig. 8, which highlights AFC cases of wallrock compositions just discussed in Fig. 7 (30:70, 50:50, 70:30, and 100:0 flysch:skarn ratios), while AFC cases of the full range of mixed wallrock compositions are shown in Supplementary Figs. 13 (70:30, 80:20, 90:10, and 100:0 flysch:skarn ratios) and 14 (30:70, 40:60, 50:50, and 60:40 flysch:skarn ratios). Compared to the FC trend of PM, AFC of the Capo d'Orlando flysch, and flysch-skarn mixtures with ≥70% flysch (Fig. 8 and Supplementary Fig. 13) induce notable increases in SiO_2 and K_2O, and decreases in TiO_2, FeO∗, CaO, and Na_2O versus MgO. The maximum concentrations of Al_2O_3 between fractionated PM derivatives and the assimilation scenarios are similar but occur at very different MgO; assimilation initially decreases Al_2O_3 compared to the FC case and delays the onset of plagioclase crystallization, which is indicated by the inflection in Al_2O_3 at ~3 wt.% MgO for most AFC cases. In addition, models that utilize this range of wallrock compositions produce nearly identical major element

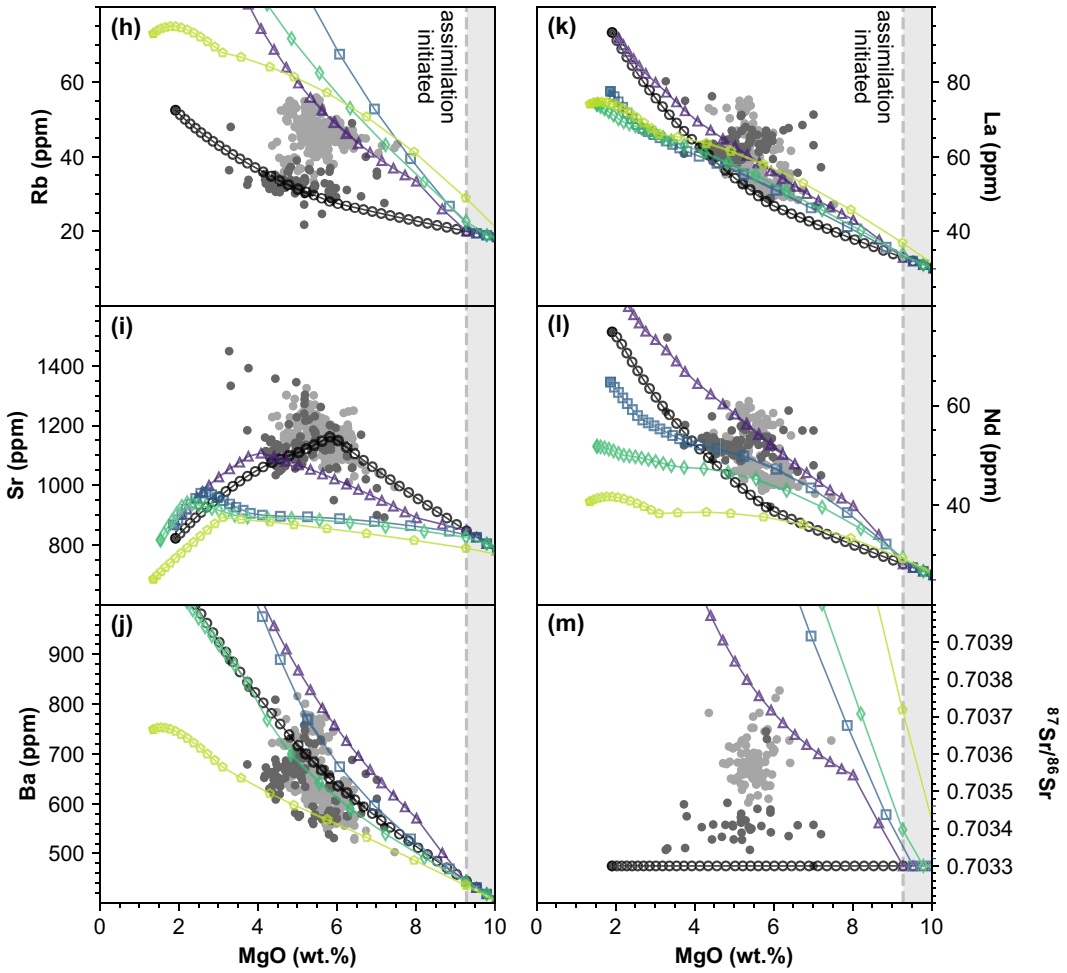

Fig. 8. Continued.

compositional trends, so it is necessary to model trace elements and $^{87}Sr/^{86}Sr$ to further evaluate model quality. These models yield magma compositions with increased Rb, La, and Nd concentrations and Sr isotope ratios, and decreased Ba concentrations (compared to the FC case). The resulting increases in Rb are in good agreement with observations, as they reach the highest observed Rb concentrations. However, the modeled $^{87}Sr/^{86}Sr$ in each of these scenarios greatly overestimate the observed values.

The four assimilation scenarios of flysch-skarn mixtures with 30% to 60% flysch (Fig. 8 and Supplementary Fig. 14) produce slightly more variation than the assimilants discussed above. Assimilation of these mixtures generates increases in SiO_2 and K_2O, and decreases in TiO_2, FeO*, CaO, and Na_2O. Mixture 1 produces the smallest increase in SiO_2 relative to the other mixtures, and the slope of its modeled K_2O trend is the closest match to observed MgO vs. K_2O; its slope is shallowest from ~6 to 4 wt.% MgO and increases more drastically at <4 wt.% MgO as the observed glass concentrations do, whereas the others increase more drastically from ~6 to 4 wt.% MgO and begin to level off at <4 wt.% MgO. Furthermore, each of these four AFC models generates increases in concentrations of Rb and Nd and in Sr isotope ratios in the contaminated melt. All models except for the 50:50 flysch:skarn mixture produce increases in Ba and La concentrations relative to simple FC. The Sr concentration behavior is more complex. The minimum peak Sr concentration reached is ~1150 ppm (30:70 mixture AFC), and the maximum is ~1300 ppm (50:50 mixture AFC), which we interpret as a function of plagioclase saturation. Sr is highly compatible in plagioclase and less compatible in the earlier phases crystallizing in these models (spinel, olivine, and clinopyroxene), and as such, Sr concentrations will increase in the melt until plagioclase saturates, at which point Sr will decrease. As a result, in the models where plagioclase saturates in the magma melt at a higher magma temperature (e.g. 30:70 mixture), a lower peak concentration of Sr is reached, whereas in the models where plagioclase saturation is delayed (e.g. 50:50 mixture), the highest peak concentrations are reached.

In summary, due to high solidi temperatures, pure skarn and interbedded flysch-skarn mixtures with ≥80% skarn are unlikely to generate substantial anatectic melt. Although assimilation of wallrock with 70% to 100% flysch produces some of the desired compositional trends, their phase assemblages are dominated by quartz, and the resulting magmas greatly overestimate SiO_2 (for a particular MgO), and high anatectic melt production due to low wallrock solidi results in exceedingly high $^{87}Sr/^{86}Sr$. As such, flysch-skarn mixtures with 30% to 60% flysch are preferred. Although a variety of these mixtures generate desired increases in K_2O and Rb concentrations and Sr isotope ratios while still producing reasonable results for parameters that are unchanged between pre- and post-1971, the 30:70 mixture as the wallrock produces the best-fit results for the combination of major oxides, trace elements, $^{87}Sr/^{86}Sr$, and phase equilibria (Mixture 1 AFC; Fig. 8).

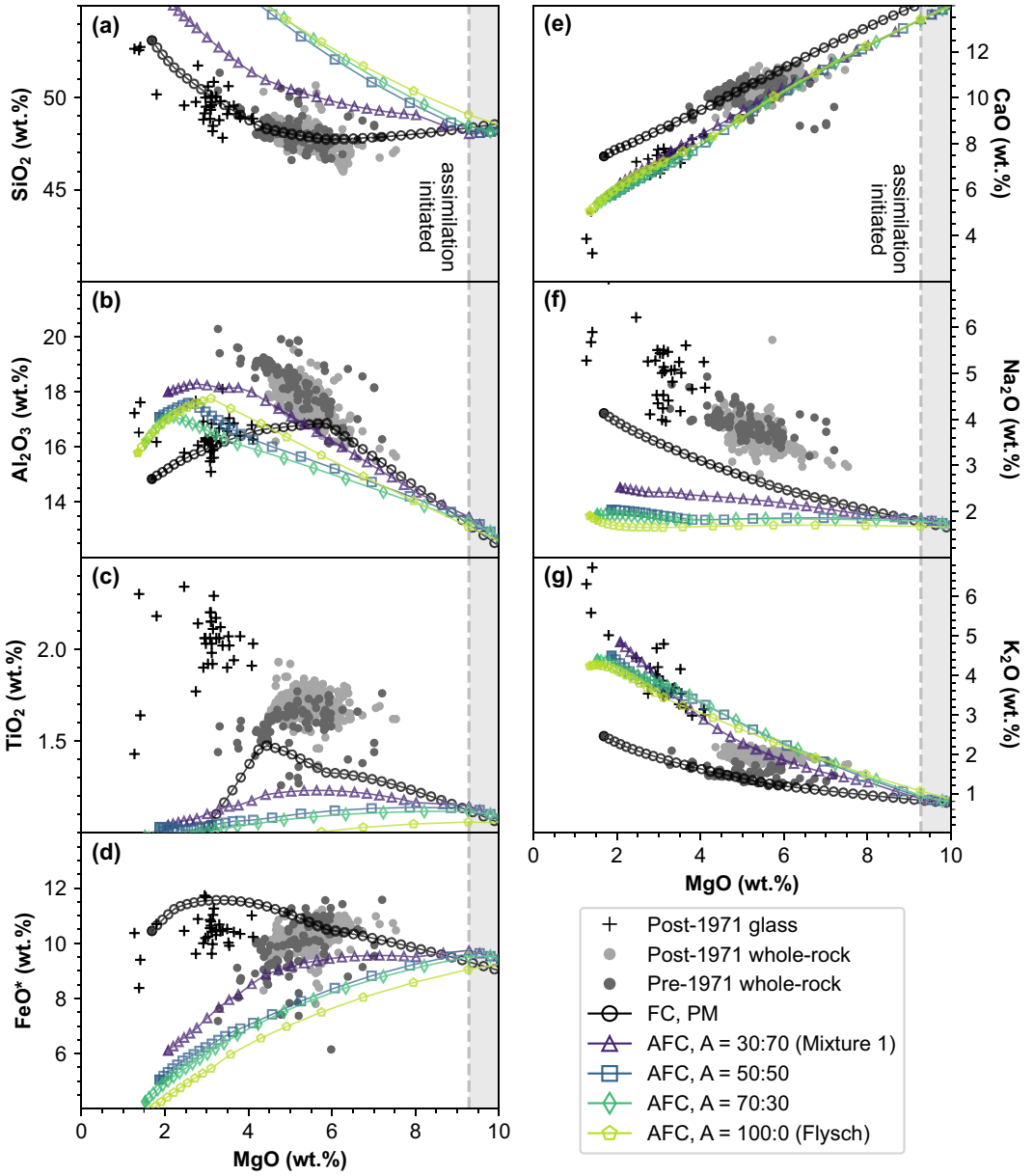

Fig. 8. Modeled AFC trends produced *via* assimilation of wallrock partial melts from the same select initial wallrock compositions shown in Fig. 7, plotted as MgO (wt.%) versus (**a**), SiO_2, (**b**) Al_2O_3, (**c**) TiO_2, (**d**) FeO∗, (**e**) CaO, (**f**) Na_2O, (**g**) K_2O (wt.%), (**h**) Rb, (**i**) Sr, (**j**) Ba, (**k**) La, (**l**) Nd (ppm), and (**m**) $^{87}Sr/^{86}Sr$. FC trend of the model PM is shown for comparison. Dashed gray line indicates the FC step after which stoping is triggered. Model progression is as described in Fig. 4. Refer to Tables 1 and 2 for initial magma and wallrock compositions. Note that partial melt assimilation of initial wallrock compositions shown with ≥50% produce models with substantial misfits for parameters such as SiO_2, Sr, and $^{87}Sr/^{86}Sr$.

MCS stoping, assimilation, and fractional crystallization (SAFC) modeling results

Although the best-fit AFC model successfully captures post-1971 compositional trends, we modeled SAFC processes to evaluate the possibility of stoping concurrent with assimilation. For consistency, we utilize Mixture 1 as both the stoped block and the wallrock that undergoes melting, since it produced the best-fit AFC model for post-1971 trends.

Compared to the best-fit AFC model, major and trace element trends that result from stoped and assimilated Mixture 1 wallrock are virtually identical (Mixture 1 SAFC, S = 2 and 5 m.u.; Fig. 9). As revealed by previous SFC models, the major limitation on stoped wallrock addition is the evolution of $^{87}Sr/^{86}Sr$ in the resident magma melt. As little as 5 m.u. of stoped Mixture 1 exceeds the observed post-1971 $^{87}Sr/^{86}Sr$ values, whereas 2 m.u. bounds the 3 most radiogenic observed samples not captured by AFC alone (Fig. 9m). These models suggest that stoping of minimal amounts of mixed flysch and skarn (e.g. 2% of the initial resident magma body mass) may accompany assimilation of anatectic melt from a similar wallrock.

DISCUSSION OF MODELS AND THEIR IMPLICATIONS

Evaluation of PM fractional crystallization model

The selected parent magma composition and its best-fit initial conditions (pressure, initial wt.% H_2O, and initial fO_2), in conjunction with information from the literature, provide constraints regarding these conditions of Etna's magmatic system. In this section, we discuss the overall fit of the models

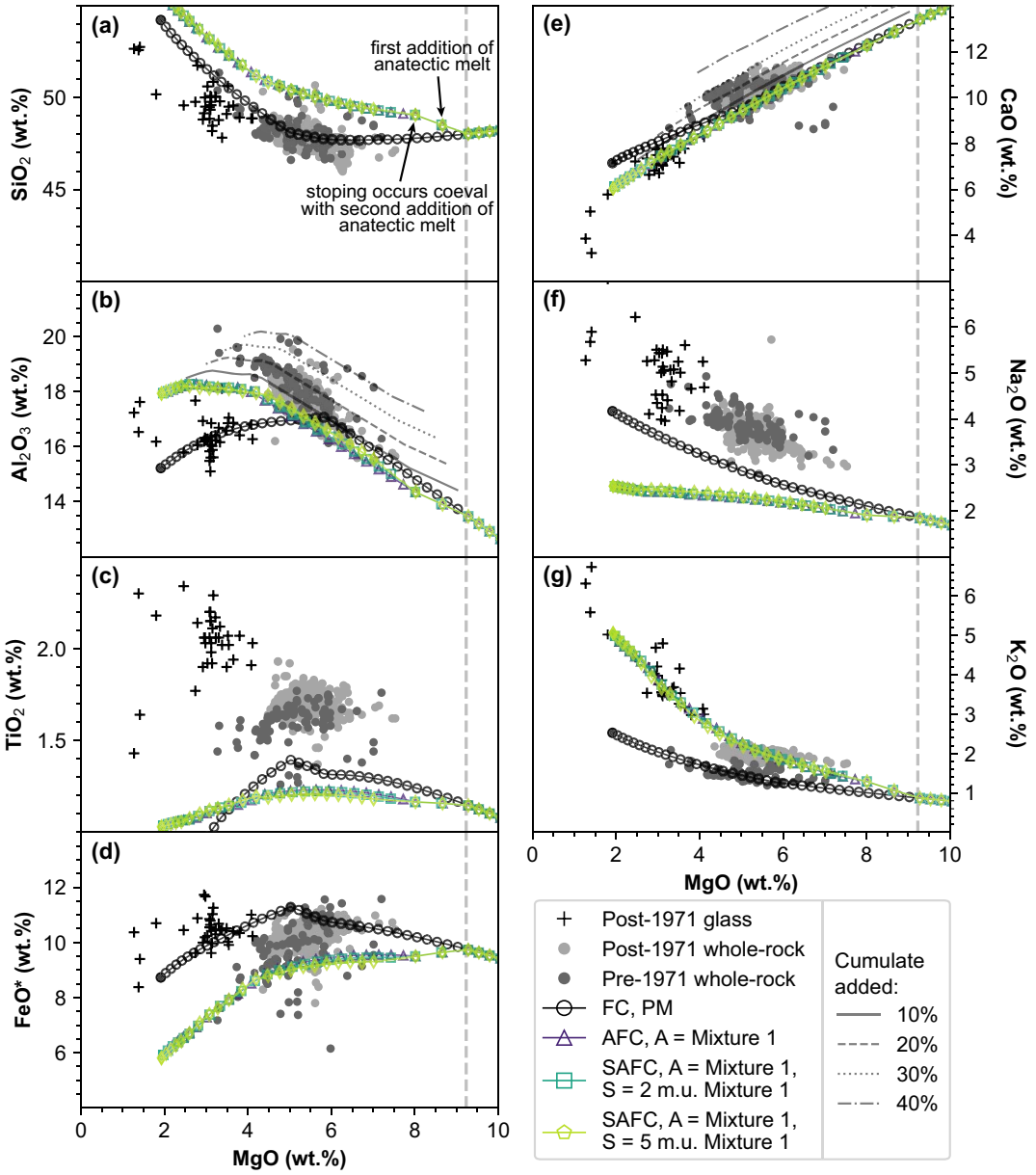

Fig. 9. AFC and SAFC trends produced *via* different initial wallrock compositions and varied stoped masses plotted as MgO (wt.%) versus (**a**) SiO_2, (**b**) Al_2O_3, (**c**) TiO_2, (**d**) FeO*, (**e**) CaO, (**f**) Na_2O, (**g**) K_2O (wt.%), (**h**) Rb, (**i**) Sr, (**j**) Ba, (**k**) La, (**l**) Nd (ppm), and (**m**) $^{87}Sr/^{86}Sr$. FC trend of the model PM is shown for comparison. Black arrows indicate the first addition of anatectic melt in the included AFC model as well as the step at which stoping occurs in the SAFC models concurrent with the second addition of anatectic melt. Contour lines show the addition of 10% to 40% of a representative cumulate to the Mixture 1 (30:70 mixture flysch:skarn) AFC model. Model progression is as described in Fig. 4. Refer to Tables 1 and 2 for initial magma and wallrock compositions. See text for model parameters and additional discussion.

and consider causes for misfits between the models and observed data.

Major oxides, trace elements, and Sr isotopes

Whereas the drivers of short-term changes like those observed in Etna's post-1971 period include chemical input from a variety of proposed sources (Clocchiatti *et al.*, 1988; Armienti *et al.*, 1989; Barbieri *et al.*, 1993; Condomines *et al.*, 1995; Tanguy *et al.*, 1997; Schiano *et al.*, 2001; Tonarini *et al.*, 2001; Viccaro & Cristofolini, 2008; Viccaro *et al.*, 2011; Viccaro & Zuccarello, 2017), FC has been invoked as the driver of Etna's geochemical characteristics over long periods of the volcano (Tanguy *et al.*, 1997). It is also noteworthy that Bohrson *et al.* (2020) show that recharge of a parent magma to a fractionated derivative magma does not profoundly affect magma compositional evolution after the initial compositional deviation (e.g. increase in MgO and decrease in SiO_2 are model outcomes to recharge but the SiO_2-MgO trend as FC occurs is similar to the trend without recharge). As such, our primary goal of defining a parent magma for this study is to identify an initial composition whose fractional crystallization evolution reproduces the compositional trends of lavas from the pre-1971 period, especially for K_2O, Rb, and $^{87}Sr/^{86}Sr$. We recognize that recharge is still occurring, but for the purposes of our study we deem models focused on FC sufficient for the pre-1971 period.

The ~4-ka FS tephra (PM; Tables 1 and 2) is selected as the parent magma because it has geochemical and petrographic characteristics akin to a primary magma (12–17 wt.% MgO, 920–1330 ppm Cr, and 135–285 ppm Ni, olivine with $Fo_{90–91}$, and clinopyroxene

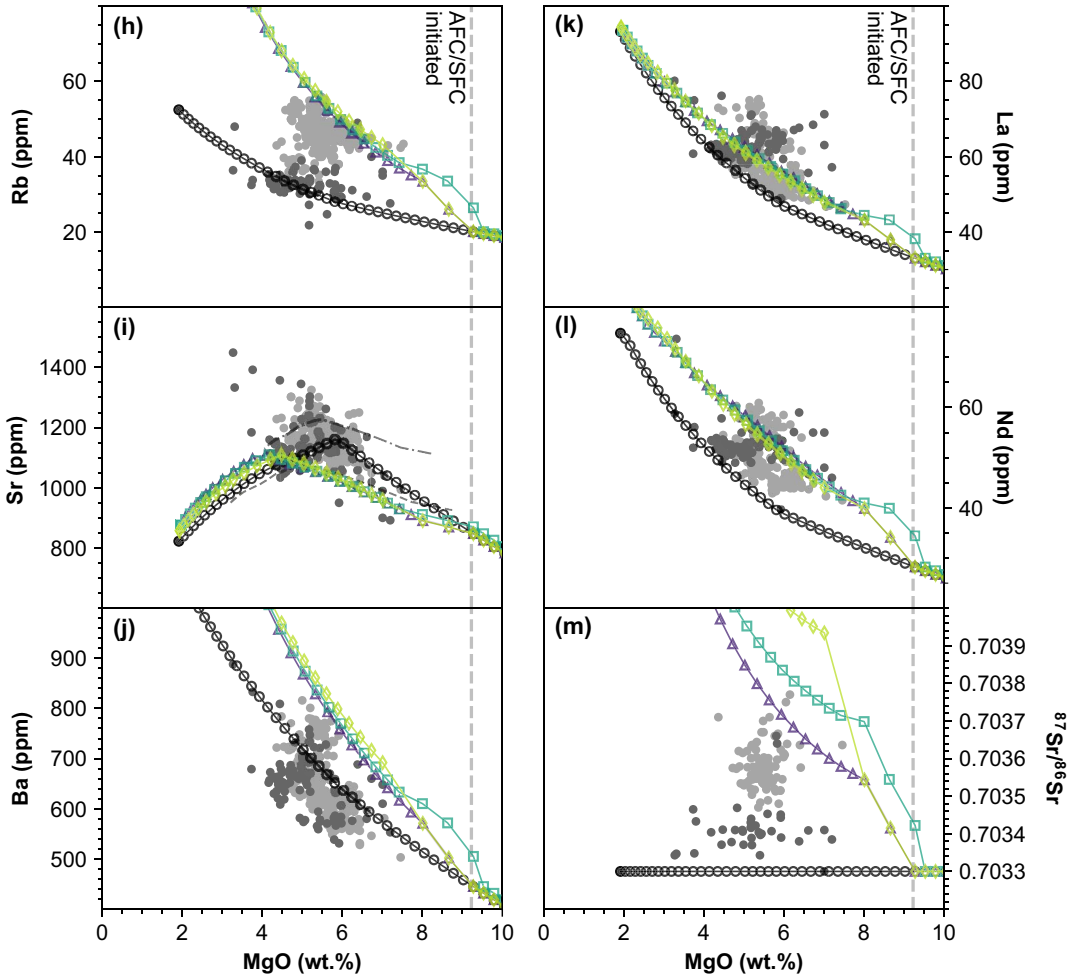

Fig. 9. Continued.

with Mg# 96–92.5), and has a low porphyritic index (<10%) so it is not heavily influenced by crystal addition. FC trends of PM successfully capture the observed pre-1971 K_2O, Rb, and $^{87}Sr/^{86}Sr$ trends, reproduce the general trends for SiO_2, Al_2O_3, FeO∗, CaO, Sr, and Ba, and define the lower limits of La and Nd versus MgO.

However, all model results (including the AFC, SFC, and SAFC scenarios) consistently underestimate Na_2O and TiO_2. We also explore three theoretical parental magmas from Viccaro & Zuccarello (2017) as alternate choices because (1) at the conclusion of FC, AFC, SFC, and SAFC modeling, it is apparent that the FS tephra chosen as the parent magma does not accurately capture whole-rock concentrations of Na_2O and TiO_2, which are underestimated in every model run; and (2) we want to briefly evaluate the range of major element compositions produced by fractional crystallization of heterogeneous mantle sources. The starting compositions for these trends use average compositions from Etna's different eruptive periods whose major and trace elements were then re-equilibrated to primary conditions by adding varied proportions of fractionated minerals in two steps (Viccaro & Zuccarello, 2017). Additional FC models using calculated compositions of primary magmas from Viccaro & Zuccarello (2017) are shown in Fig. 10 (VZ2017). Notably, using these primary magma compositions that represent different periods of Etna's activity, the models still fail to capture most observed TiO_2 trends. In addition, these models, which capture the range of observed Na_2O, illustrate that the initial Na_2O composition of Etna's ~4-ka FS tephra is likely not representative of magmas generated over the 1329 to 2005 period. A magma with an additional ~1 wt % Na_2O is a more likely primary composition, as illustrated by FC trends of VZ2017 primary magmas. In comparison to FC of PM, the trends of VZ2017 magmas capture a similar range of values for SiO_2, Al_2O_3, CaO, and FeO∗. The Al_2O_3 trends differ slightly based on the timing of plagioclase saturation noted by the inflection point. The trend of 'ET-75' and 'Pre-1971' compositions capture observed pre-1971 variability in terms of K_2O in addition to PM. The 'Post-1971' initial composition produces a fractionation trend that is the most K-enriched of all FC trends and captures the lowest values of observed post-1971 samples, but still fails to capture the datapoints most enriched in K_2O. These results suggest that: (1) the mismatch of modeled and observed TiO_2 versus MgO for all trends may be rooted in the control of fO_2 on modeled Fe-Ti oxides, (2) the primary melts generated to produce the 1329 to 2005 CE magmas are higher in Na_2O contents compared to those from the ~4-ka FS tephra, (3) the variability in the data captured by these alternative parent magmas is consistent with the suggestion that Etna is sourced by heterogeneous mantle (e.g. Viccaro & Cristofolini, 2008; Viccaro *et al.*, 2011; Viccaro & Zuccarello, 2017), and (4) although FC of the 'Post-1971' initial composition captures the least K-enriched post-1971 lavas, the range of mantle heterogeneity represented by these samples is insufficient to perfectly explain the majority of enriched post-1971 lavas.

There is also an inherent limitation when comparing MCS modeled data to observed whole-rock data. MCS utilizes batch fractional crystallization, in which crystal phases are removed

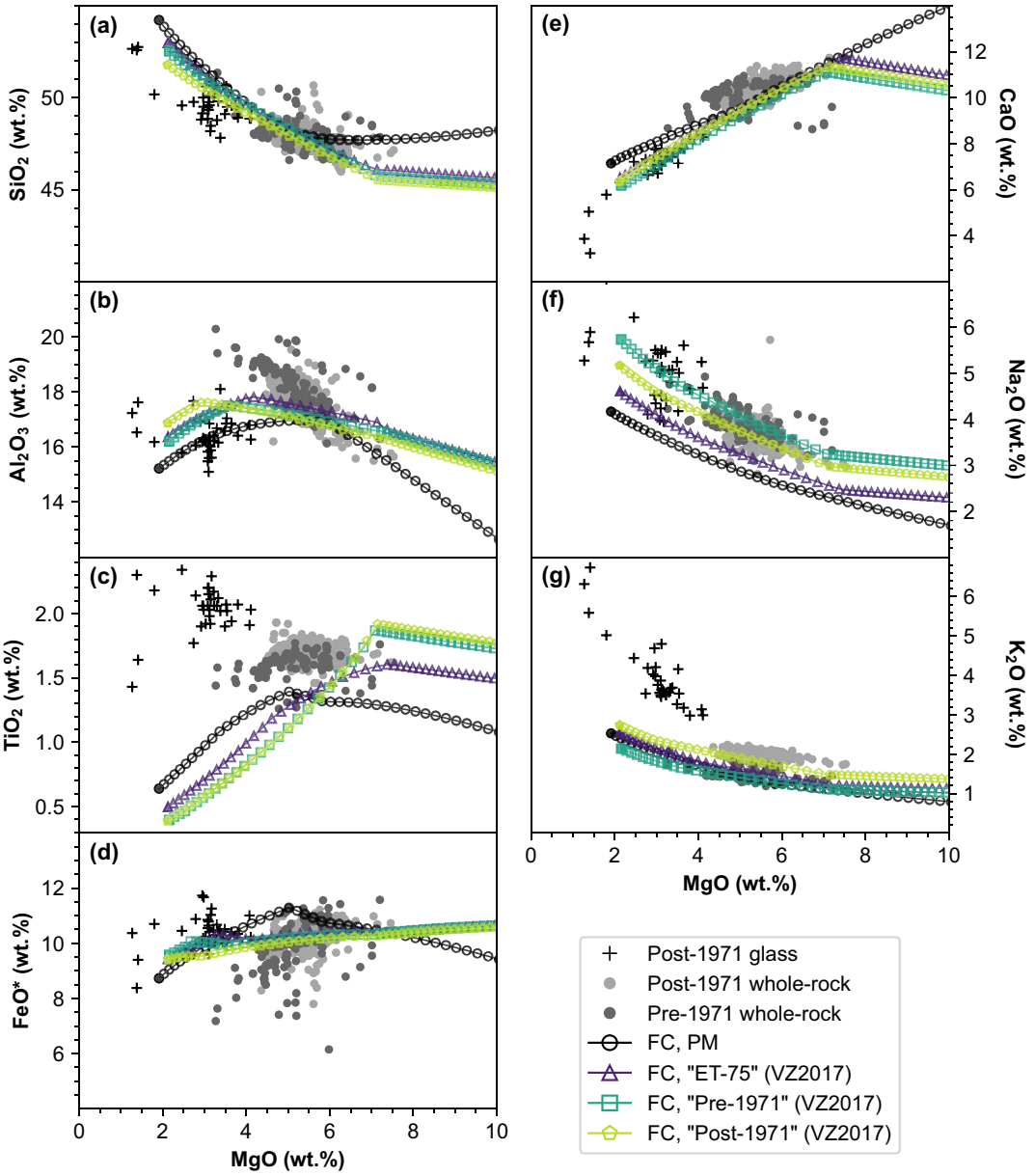

Fig. 10. MCS major element FC trends of model PM and alternative parent magma compositions from Viccaro & Zuccarello (2017) (indicated by VZ2017) compared to observed data shown for MgO (wt.%) versus (**a**) SiO_2, (**b**) Al_2O_3, (**c**) FeO*, (**d**) TiO_2, (**e**) CaO, (**f**) Na_2O, and (**g**) K_2O (wt.%). Refer to Table 1 for initial magma compositions.

at each temperature decrement into a cumulate reservoir that interacts thermally but not chemically with the resident magma melt. As such, the model records the compositional evolution of the melt as the resident magma body cools at an incremental temperature step. This step-by-step compositional evolution of the melt is then compared to observed whole-rock data, which is a straightforward comparison if observed data are taken from glass compositions or largely aphyric rocks. However, in samples where the porphyritic index is greater than ~10%, the chemical effects of crystals need to be evaluated to assess modeled versus observed data fit.

For eruptions between 1329 and 2005 CE, lavas typically exhibit 10% to 40% phenocrysts by volume (e.g. Armienti *et al.*, 1994b; Corsaro *et al.*, 2007, 2009; Viccaro & Cristofolini, 2008; Ferlito *et al.*, 2009; De Beni *et al.*, 2011), and infrequently >40 vol.% (e.g. Viccaro & Cristofolini, 2008; Kahl *et al.*, 2017). No models, including the best-fit AFC model, reach the upper limits of observed Al_2O_3, CaO, and Sr data. To evaluate if the porphyritic nature of the samples can explain the misfits in these elements, we calculated a bulk cumulate composition based on the average mineral proportions (63% plagioclase, 30% clinopyroxene, 7% olivine) taken from the literature for the 1977 to 2005 eruptions (Electronic Appendix 2), and major oxide mineral compositions taken from the average of all FC steps with a melt composition in the range of ~2 to 8 wt.% MgO in the best-fit AFC model. Mineral trace element concentrations were estimated based on GEOROC mineral compilations. Plagioclase trace element concentrations from the GEOROC database were specifically averaged from Etnean trachybasalts from 1600 to 2005 CE (Viccaro *et al.*, 2016), whereas olivine and clinopyroxene trace element estimates included an average of all trachybasaltic rocks in the GEOROC mineral data compilation due to a lack of available trace element data for Etna-specific samples (Electronic Appendix 2). The Sr isotope value of the cumulate was estimated based on the least radiogenic sample in the data collection

(Electronic Appendix 1). Figure 9b, e, i illustrates cumulate + AFC melt mixtures where cumulates comprise up to 40% of the mixture for Al_2O_3, CaO, and Sr versus MgO.

The addition of variable crystal assemblages produces predictable effects due to the plagioclase-rich nature of the cumulate (Fig. 9): increased Al_2O_3, CaO, and Sr. To reach the upper limit of Al_2O_3, CaO, and Sr, the best-fit SAFC scenario required the addition of approximately 40% of the defined cumulate for Al_2O_3 and 30% for CaO. Most Sr concentrations can be explained by the addition of 40% of the cumulate, however, a subset of data lies above the 40% contour line. Major oxide and trace element concentrations and Sr isotope ratios above and below the best-fit AFC and SAFC MCS models can, therefore, be explained by the addition of up to approximately 40% of a plagioclase-dominated + clinopyroxene + olivine phase assemblage. This result is consistent with the upper limit of the modes of these rocks and strengthens the suggestion that assimilation plus a small degree of stoping are critical processes in the post-1971 magmas in addition to heterogeneities inherited directly from the mantle source.

Is crustal contamination a plausible explanation for the alkali enrichment trend?

Although direct modeling of magma-carbonate interactions was not successful in this study, petrological and experimental studies provide insight into the potential outcomes of this process. Various studies suggest a magma contaminated by carbonate would undergo increases in $^{87}Sr/^{86}Sr$ (Del Moro *et al.*, 2001; Chadwick *et al.*, 2007; Iacono Marziano *et al.*, 2008; Deegan *et al.*, 2010; Di Rocco *et al.*, 2012; Borisova *et al.*, 2013; Jolis *et al.*, 2013) and concentrations of CO_2 (Iacono Marziano *et al.*, 2008, 2009; Deegan *et al.*, 2010; Mollo *et al.*, 2010; Di Rocco *et al.*, 2012; Borisova *et al.*, 2013; Heap *et al.*, 2013; Jolis *et al.*, 2013), as well as contain Ca-rich melt and/or crystals including clinopyroxene (Iacono Marziano *et al.*, 2007, 2008; Deegan *et al.*, 2010; Jolis *et al.*, 2013). However, carbonate rocks are unlikely to survive extended interaction with magma. The suggestion that skarn may be the prevalent form of carbonate contemporaneous with the evolution of post-1971 magmas is supported by metamorphosed carbonate xenoliths found at Etna and other volcanoes with carbonate basements worldwide (Michaud, 1995; Iacono Marziano *et al.*, 2007; Di Rocco *et al.*, 2012; Jolis *et al.*, 2015), and clinopyroxene with highly radiogenic Sr values also provide compelling evidence that magma-carbonate interaction has occurred (Nelson, 2015).

Partial melts of skarn and flysch-skarn mixtures with 80% to 90% skarn are unlikely assimilants. Rhyolite-MELTS models establish a range of skarn solidi values from 1145 °C to 1193 °C. Assimilation and FC of PM (T_{liq} = 1361 °C) with skarn wallrock fails to yield reasonable results for the range of compositions seen in the post-1971 Etna samples; magma and wallrock consistently reach thermal equilibrium before wallrock melts are produced. It is, therefore, unlikely, based on thermodynamic restrictions, that these highly restitic skarns could melt efficiently enough to be assimilated and cause the substantial geochemical changes observed in post-1971 lavas. Flysch and flysch-dominated mixtures are eliminated as both a stoped and assimilated component, as they yield models that drastically overestimate SiO_2 and $^{87}Sr/^{86}Sr$ (Figs. 5 and 6).

Nelson (2015) documents clinopyroxene $^{87}Sr/^{86}Sr$ values as high as 0.710207 ± 0.000063, which is interpreted as evidence for the stoping of the sedimentary basement into post-1971 Etnean lavas, as clinopyroxene is a major phase in skarn-dominated wallrock, and composite xenoliths documented in Etnean lavas flows represent the heterogenous nature of the crust beneath Etna (Michaud, 1995). Based on these models, mixtures of skarn and flysch may form the dominant wallrock for the shallow crustal Etna magma storage zone. The assimilation of partial melts generated from flysch-skarn mixtures (excluding those with ≥80% skarn) yield magma compositions with elevated K_2O and Rb concentrations and $^{87}Sr/^{86}Sr$. The skarns beneath Etna have radiogenic Sr values akin to the seawater at the time of their sedimentary protolith formation in the Cretaceous to Jurassic periods. Sr isotope values of skarns in this study were estimated at 0.7075 based on the seawater curve of McArthur *et al.* (2001), and the Capo d'Orlando flysch has a value measured at 0.71776 (Table 2). Mixtures of these endmembers thus have Sr isotopic values between these two, with the best fit assimilant having $^{87}Sr/^{86}Sr$ of 0.7128 (Mixture 1). Therefore, assimilation raises the Sr isotope values of the resident melt as magma evolution progresses. Furthermore, partial melts of these wallrocks are high in Rb (up to ~800 ppm) and K_2O (up to ~12 wt.%) (Fig. 7), which causes significant increases in the Rb and K_2O concentrations in the corresponding contaminated magma melts. We interpret the high concentrations of K_2O and Rb in the partial melts to be the result of the mineralogy of these wallrocks. The flysch-skarn mixtures all contain K-feldspar and biotite, which are rich in K and Rb. As the magma delivers enthalpy to the wallrocks and the wallrock temperatures increased, these minerals melt completely over the course of the model runs. Therefore, the partial melts of flysch-skarn wallrocks are rich in K, Rb, and have relatively radiogenic Sr, and *via* their assimilation, the resident magma body is enriched in these elements and Sr isotopes. The results of this process coincide well with the post-1971 trends observed at Etna. The sensitivity of $^{87}Sr/^{86}Sr$ in the models places a general limit on the mass of stoped material of ~2% of the magma body mass when stoping occurs in conjunction with assimilation. This amount of skarn or skarn-dominated mixtures, for various compositions, can be added to the modeled magma melt and still maintain the general major oxide and trace element trends observed in Etnean lavas while not exceeding the observed Sr isotopes (Fig. 9).

Based on the best-fit open-system model, crust-magma interaction beneath Etna likely involves assimilation ± minor stoping of wallrock (Fig. 9) in addition to FC. Best-fit results yield mass estimates that indicate the crustal contribution is likely to be <20% of the initial magma body mass (e.g. ~2 m.u. of stoped wallrock and ~17 m.u. of assimilated partial melts). However, reference to Fig. 9 shows that this model does not capture the entire post-1971 data set for any element or oxide. The most likely explanation is that the sedimentary substrata beneath Etna are heterogeneous; crustal xenoliths described by Michaud (1995) exhibit heterogeneity in their geochemistry and phase assemblages, as do carbonate xenoliths at other Italian volcanoes such as Vesuvius (Jolis *et al.*, 2015) and the Colli Albani district (Di Rocco *et al.*, 2012). Consistent with this suggestion, sensitivity models demonstrate that different wallrock compositions yielded different model outcomes. The skarn utilized in flysch-skarn wallrock combinations is Skarn 1 (Tables 1 and 2). Many eliminated skarn xenolith compositions had comparatively lower SiO_2 values (~7–34 wt.%). Mixing a lower SiO_2 skarn composition with the Capo d'Orlando flysch (SiO_2 = 69.7 wt.%) would reduce the amount of SiO_2 in the wallrock, while retaining the necessary elevated K_2O that the skarns provide. Such heterogeneity could explain the overestimation of SiO_2 that results from the assimilation of partial melts from flysch-dominated wallrock mixtures. Similarly, wallrock mixtures dominated by the Capo d'Orlando flysch tend

to overestimate Sr isotope values. The estimated $^{87}Sr/^{86}Sr$ ratio of the skarns used in this study (0.7075) is taken from the Sr isotope seawater curve of McArthur *et al.* (2001) and represents a mid-range seawater value for the Cretaceous period in which most of the carbonates in the Hyblean Plateau formed. However, some of the carbonate rocks of the Hyblean Plateau may have formed as far back as the Jurassic period, where Sr isotope seawater values reached as low as ~0.7068. Invoking variable $^{87}Sr/^{86}Sr$ to reflect the heterogeneity of the seawater curve over the time periods in which the carbonate protoliths were deposited may explain the mismatch between the modeled and observed Sr isotope data.

A model for the alkali enrichment trend at Etna

Together, FC of PM and the best-fit AFC/SAFC models effectively bracket the observed pre- and post-1971 whole-rock data (Fig. 9). This holds especially true for K_2O, Rb, and $^{87}Sr/^{86}Sr$, where PM defines the lower limit of concentrations (i.e. pre-1971 data) and the AFC/SAFC models define the upper limit of concentrations (i.e. post-1971 data). In this section, we discuss a model for the Etnean magmatic storage and transport system based on these models coupled with information gleaned from the literature.

A variety of studies have identified characteristics of Etna's magma storage and transport system in the lower- to upper-crust (Sharp *et al.*, 1980; Trigila *et al.*, 1990; Murru *et al.*, 1999; Chiarabba *et al.*, 2000, 2004; Armienti *et al.*, 2004, 2007; Bonforte *et al.*, 2008; Nelson, 2015; Giuffrida & Viccaro, 2017; Ubide & Kamber, 2018; Giuffrida *et al.*, 2023). Significantly, these studies place the upper crustal portions of Etna's magmatic transport and storage system within the sedimentary basement (<10–15 km depth). Further evidence for the direct interaction between the sedimentary basement and Etnean magmas is recorded by sedimentary xenoliths, which are generally sampled during ascent of magma. Michaud (1995) carried out a systematic mineralogical and geochemical study on xenoliths and their host magmas from the 1892, 1986, and 1989 Etnean lavas. The xenoliths are categorized into siliceous, peraluminous, carbonate, and composite types, reflecting the highly heterogeneous nature of the sedimentary basement, and show evidence of morphological, structural, mineralogical, and geochemical alterations, which were likely induced by thermal and chemical exchanges with the host magma. Michaud (1995) also recognized early and strong mobility of K, Rb, and Cs from the xenolith toward its corresponding anatectic melt and enclosing lava, which identifies these crustal rocks as a potential source of alkali elements.

The location of the storage and transport system, along with evidence from sedimentary-metamorphic xenoliths documented at Etna, indicate that magmas are indeed in direct contact and interact physically and chemically with the flysch and carbonate/skarn substrata. The complex nature of the present storage and transport system as a plexus of dikes and sills (Trigila *et al.*, 1990; Armienti *et al.*, 2004; Chiarabba *et al.*, 2004; Corsaro & Pompilio, 2004c; Andronico *et al.*, 2005; Corsaro *et al.*, 2007) creates even larger areas of contact (compared to a single, large magma chamber) between the magma and wallrock to support these thermal and chemical exchanges.

1329–1971 CE

Based on the best-fit FC model of PM, we suggest that the geochemical signature of lavas in the pre-1971 magma transport and storage system was dominated by the supply of a magma similar to the ~4-ka FS tephra, a composition that Kamenetsky *et al.* (2007) postulates to be the type of magma supplying more recent eruptions. The major oxide (except Na_2O and TiO_2), trace element, and Sr isotope characteristics of lavas emitted from 1329 to 1971 can generally be replicated by FC of a parent magma that is a high-Mg (12–17 wt.% MgO) basalt to picrite composition (PM), which has lost part of its pristine volatile cargo through degassing and, therefore, has an initial H_2O content of 1.0 wt.% at a pressure of ~0.2 GPa. The early fractionation of olivine and clinopyroxene in MCS models drives the basaltic magma to trachybasalt and basaltic-trachyandesite compositions, which are the dominant rock types during this period. This magma rose through the crust and was eventually stored in the upper crust, at ~6 km depth (Fig. 1c). The magma bodies in the complex storage and transport system were delivering enthalpy to the surrounding wallrock. During this period, we suggest that interactions between the magma and sedimentary crust were dominated by thermal exchange but mass transfer (i.e. assimilation and stoping) was not a dominant process. Perhaps, this phase represents the heating of wallrock from low ambient temperatures to higher values approaching the solidus. This pre-heating history is a requirement because ambient crustal temperatures before magma intrusion were ~200 °C to 300 °C, far below the solidus.

Clinopyroxene, a common phase in skarns (including those modeled here), are identified with high $^{87}Sr/^{86}Sr$ in the eruptions of 1886 and 2004, which suggest magmatic skarn was present in the surrounding wallrock and later incorporated into these magma bodies (Nelson, 2015). Furthermore, pre-1971 whole-rock Sr isotopes display slight variations (~0.7033–0.7035) (Fig. 2e). As discussed above, FC models for this period are sufficient for the purposes of this work, but differences over a range of 0.0002 $^{87}Sr/^{86}Sr$ documented in pre-1971 magmas suggest recharge of magmas with modest isotopic variability was also occurring. Viccaro & Cristofolini (2008) ascribe this to partial melting of a heterogeneously enriched mantle by ancient metasomatic events where increased melting of phlogopite, which may have undergone time-integrated increases in radiogenic Sr, can contribute to increases in $^{87}Sr/^{86}Sr$.

1971–2005 CE

Conversely, crustal assimilation is a significant process recorded in post-1971 lavas. The major and trace element and isotopic characteristics of lavas emitted from 1971 to 2005 CE can be generally replicated *via* assimilation and stoping of the sedimentary basement by a parent magma similar to that of the pre-1971 magma system. Upper crustal skarn and flysch contain elevated abundances of alkali elements (K, Rb, Cs) and radiogenic Sr (Del Moro *et al.*, 2001; McArthur *et al.*, 2001; Mikes *et al.*, 2006; Di Rocco *et al.*, 2012), and thermal and chemical interactions between the wallrock and Etnean magmas have the demonstrated potential (Michaud, 1995) to exchange these alkali elements *via* anatectic melts or fluid phases (Clocchiatti *et al.*, 1988). Additionally, Chiodini *et al.* (2011) document a shift to heavier $\delta^{13}C$ isotopes (−4‰ in the 1970s and 1980s to −1‰ in 2009) from CO_2 measurements in Etna's volcanic gas plumes, which is consistent with carbonate assimilation.

By 1971, we speculate that the wallrock was thermally primed to undergo partial melting sufficient to generate the observed geochemical signatures *via* their assimilation into the resident magmas. During this time, recharge magmas of variable compositions mixing with resident magmas also may supply some of the heterogeneity in the observed Etnean lavas (Fig. 10). Partial melting of mantle material heterogeneously containing phlogopite,

which has higher partition coefficients for K and Rb than other mantle minerals, should produce magmas relatively enriched in these elements as well as $^{87}Sr/^{86}Sr$ (Viccaro & Cristofolini, 2008; Viccaro & Zuccarello, 2017). Casetta *et al.* (2019) also highlight the importance of phlogopite and amphibole in Etna's mantle source, but instead invoke a modally and compositionally homogenous mantle domain melted to different degrees. Either way, variations in magmas supplied by the mantle are likely to generate a degree of heterogeneity *via* recharge magmas. Magma recharge can also enhance crustal assimilation by supplying additional heat to the surrounding wallrock (e.g. see RAFC examples in Bohrson *et al.*, 2020). Nelson (2015) recorded post-1971 sample rims that are more enriched in radiogenic Sr than their cores, implying that the alkali enrichment event is a late-stage process, and proposed that an increase in the rates of magma recharge can enhance the assimilation process as well. This idea is also supported by experimental studies, such as Iacono Marziano *et al.* (2008), that demonstrated limestone assimilation can be induced by interaction with a hot, mafic melt.

Based on the results of >300 MCS models that evaluate whole-rock major oxides, trace elements and Sr isotopes, and mineral assemblage identity, composition, and abundance, late-stage crustal contamination by heterogeneous mixtures of skarn and flysch contributes to the mass balance of the enrichment in alkali elements and radiogenic Sr, in conjunction with geochemical variations introduced by a heterogeneous mantle *via* recharge/-magma mixing. Crustal heterogeneity is indirectly supported by the modeling results, which, even in the case of the best-fit model, do not capture all observed whole-rock and mineral data. The suggestion that the magma storage system is a plexus of dikes and sills is also supported by the variability of the observed data, even within a single eruption (e.g. Behncke & Neri, 2003; Clocchiatti *et al.*, 2004; Andronico *et al.*, 2005; Viccaro *et al.*, 2006; Ferlito *et al.*, 2012; Magee *et al.*, 2021). The complex nature of the magma storage system can allow magmas to be stored in physically isolated chambers, which can interact with spatially heterogeneous wallrock compositions or mix with varied recharge magmas, which means these magma chambers are not equally affected by fractionation and other open-system processes (e.g. recharge and assimilation).

CONCLUDING REMARKS

This research demonstrates the utility of the Magma Chamber Simulator to model crustal contamination processes *via* its application to Mt. Etna volcano. Quantifying crustal input from 1329 to 2005 CE provides insight into the physical and chemical shift that occurred in post-1971 Etnean lavas, which includes an intriguing enrichment in alkali elements and radiogenic Sr, and an increase in the volume, frequency, and explosivity of eruptions. The pre-1971 magma storage and transport system is dominated by magmas similar to those observed in the ~4-ka FS tephra. Thermal interactions stimulated by repeated recharge of hot, mafic magmas induced melting and reaction of the sedimentary crust. By 1971 the wallrock was primed for a sufficient amount of assimilation that could cause the observed increases in K_2O, Rb, and $^{87}Sr/^{86}Sr$. The post-1971 magma storage and transport system thus included flysch and carbonate assimilation and stoping, which is a contributor to the post-1971 alkali enrichment. The crustal signature causing the alkali enrichment is in conjunction with the signature of mantle heterogeneity. Thorough modeling studies such as this may prove useful at other volcanoes where crustal contamination is suggested.

ACKNOWLEDGEMENTS

Many thanks to Jenna V. Adams and Garrett Zeff for assistance with initial rhyolite-MELTS and MCS modeling. Reviews by Emanuela Gennaro, Ana Martinez-Ardila, and an anonymous reviewer helped to improve the clarity of the original manuscript.

FUNDING

This work was supported by the National Science Foundation (1551052 and 2151038 to W.A.B.; 2151039 to F.J.S), Central Washington University, Colorado School of Mines, and University of California-Santa Barbara. The authors have no relevant financial or non-financial interests to disclose.

DATA AVAILABILITY

The data underlying this article are available in its online supplementary material.

References

Andronico, D. & Corsaro, R. A. (2011). Lava fountains during the episodic eruption of south-east crater (Mt. Etna), 2000: insights into magma-gas dynamics within the shallow volcano plumbing system. *Bulletin of Volcanology* **73**, 1165–1178. https://doi.org/10.1007/s00445-011-0467-y.

Andronico, D., Branca, S., Calvari, S., Burton, M., Caltabiano, T., Corsaro, R. A., del Carlo, P., Garfì, G., Lodato, L., Miraglia, L., Murè, F., Neri, M., Pecora, E., Pompilio, M., Salerno, G. & Spampinato, L. (2005). A multi-disciplinary study of the 2002-03 Etna eruption: insights into a complex plumbing system. *Bulletin of Volcanology* **67**, 314–330. https://doi.org/10.1007/s00445-004-0372-8.

Armienti, P., Innocenti, F., Petrini, R., Pompilio, M. & Villari, L. (1989). Petrology and Sr-Nd isotope geochemistry of recent lavas from Mt. Etna: bearing on the volcano feeding system. *Journal of Volcanology and Geothermal Research* **39**, 315–327. https://doi.org/10.1016/0377-0273(89)90095-4.

Armienti, P., Clocchiatti, R., D'Orazio, M., Innocenti, F., Petrini, R., Pompilio, M., Tonarini, S. & Villari, L. (1994a). The long-standing 1991-1993 Mount Etna eruption: petrography and geochemistry of lavas. *Journal of the National Volcanic Group of Italy* **4**, 15–28.

Armienti, P., Pareschi, M. T., Innocenti, F. & Pompilio, M. (1994b). Effects of magma storage and ascent on the kinetic of crystal growth. *Contributions to Mineralogy and Petrology* **115**, 402–414. https://doi.org/10.1007/BF00320974.

Armienti, P., Tonarini, S., D'Orazio, M. & Innocenti, F. (2004). Genesis and evolution of Mt. Etna alkaline lavas: petrological and Sr-Nd-B isotope constraints. *Per. Mineral.* **73**, 29–52.

Armienti, P., Tonarini, S., Innocenti, F. & D'Orazio, M. (2007). Mount Etna pyroxene as tracer of petrogenetic processes and dynamics of the feeding system. *Special Paper 418: Cenozoic Volcanism in the Mediterranean Area 2418* , 265–276. https://doi.org/10.1130/2007.2418(13).

Asimow, P. D. & Ghiorso, M. S. (1998). Algorithmic modifications extending MELTS to calculate subsolidus phase relations. *American Mineralogist* **83**, 1127–1132. https://doi.org/10.2138/am-1998-9-1022.

Barbieri, M., Cristofolini, R., Delitala, M. C., Fornaseri, M., Romano, R., Taddeucci, A. & Tolomeo, L. (1993). Geochemical and Sr-isotope data on historic lavas of Mount Etna. *Journal of Volcanology and Geothermal Research* **56**, 57–69. https://doi.org/10.1016/0377-0273(93)90050-2.

Behncke, B. & Neri, M. (2003). The July-august 2001 eruption of Mt. Etna (Sicily). *Bulletin of Volcanology* **65**, 461–476. https://doi.org/10.1007/s00445-003-0274-1.

Bohrson, W. A., Spera, F. J., Ghiorso, M. S., Brown, G. A., Creamer, J. B. & Mayfield, A. (2014). Thermodynamic model for energy-constrained open-system evolution of crustal magma bodies undergoing simultaneous recharge, assimilation and crystallization: the magma chamber simulator. *Journal of Petrology* **55**, 1685–1717. https://doi.org/10.1093/petrology/egu036.

Bohrson, W. A., Spera, F. J., Heinonen, J. S., Brown, G. A., Scruggs, M. A., Adams, J. V., Takach, M. K., Zeff, G. & Suikkanen, E. (2020). diagnosing open-system magmatic processes using the magma chamber simulator (MCS): part I—major elements and phase equilibria. *Contribution to Mineralogy and Petrology* **175**, 1–29. https://doi.org/10.1007/s00410-020-01722-z.

Bonforte, A., Bonaccorso, A., Guglielmino, F., Palano, M. & Puglisi, G. (2008). Feeding system and magma storage beneath Mt. Etna as revealed by recent inflation/deflation cycles. *Journal of Geophysical Research* **113**, 1–13. https://doi.org/10.1029/2007JB005334.

Borgia, A., Ferrari, L. & Pasquarè, G. (1992). Importance of gravitational spreading in the tectonic and volcanic evolution of Mount Etna. *Nature* **357**, 231–235. https://doi.org/10.1038/357231a0.

Borisova, A. Y., Martel, C., Gouy, S., Pratomo, I., Sumarti, S., Toutain, J. P., Bindeman, I. N., de Parseval, P., Metaxian, J. P. & Surono (2013). Highly explosive 2010 Merapi eruption: evidence for shallow-level crustal assimilation and hybrid fluid. *Journal of Volcanology and Geothermal Research* **261**, 193–208. https://doi.org/10.1016/j.jvolgeores.2012.11.002.

Bousquet, J. C. & Lanzafame, G. (2004). The tectonics and geodynamics of Mt. Etna: synthesis and interpretation of geological and geophysical data. *Mt. Etna: Volcano Laboratory* **143**, 29–47. https://doi.org/10.1029/143GM03.

Bragagni, A., Mastroianni, F., Münker, C., Conticelli, S. & Riccardo Avanzinelli, R. (2022). A carbon-rich lithospheric mantle as a source for the large CO_2 emissions of Etna volcano (Italy). *Geology* **50**, 486–490. https://doi.org/10.1130/G49510.1.

Branca, S. & Del Carlo, P. (2004). Eruptions of Mt. Etna during the past 3,200 years: a revised compilation integrating the historical and stratigraphic records. *Mt. Etna: Volcano Laboratory* , 1–27.

Branca, S. & Del Carlo, P. (2005). Types of eruptions of Etna volcano AD 1670-2003: implications for short-term eruptive behaviour. *Bulletin of Volcanology* **67**, 732–742. https://doi.org/10.1007/s00445-005-0412-z.

Branca, S., Coltelli, M. & Groppelli, G. (2011a). Geological evolution of a complex basaltic volcano: Mount Etna, Italy. *Italian Journal of Geosciences* **130**, 306–317. https://doi.org/10.3301/IJG.2011.13.

Branca, S., Coltelli, M., Groppelli, G. & Lentini, F. (2011b). Geological map of Etna volcano, 1:50,000 scale. *Italian Journal of Geosciences* **130**, 265–291. https://doi.org/10.3301/IJG.2011.15.

Cannata, A., Di Grazia, G., Giuffrida, M., Gresta, S., Palano, M., Sciotto, M., Viccaro, M. & Zuccarello, F. (2018). Space-time evolution of magma storage and transfer at Mt. Etna volcano (Italy): the 2015-2016 reawakening of Voragine crater. *Geochemistry, Geophysics, Geosystems* **19**, 471–495. https://doi.org/10.1002/2017GC007296.

Casetta, F., Giacomoni, P. P., Ferlito, C., Bonadiman, C. & Coltorti, M. (2019). The evolution of the mantle source beneath Mt. Etna (Sicily, Italy): from the 600 ka tholeiites to the recent trachybasaltic magmas. *International Geology Review. Taylor & Francis*, 1–22.

Catalano, S., Torrisi, S. & Ferlito, C. (2004). The relationship between Late Quaternary deformation and volcanism of Mt. Etna (eastern Sicily): new evidence from the sedimentary substratum in the Catania region. *Journal of Volcanology and Geothermal Research* **132**, 311–334. https://doi.org/10.1016/S0377-0273(03)00433-5.

Chadwick, J. P., Troll, V. R., Ginibre, C., Morgan, D. J., Gertisser, R., Waight, T. E. & Davidson, J. P. (2007). Carbonate assimilation at Merapi volcano, Java, Indonesia: insights from crystal isotope stratigraphy. *Journal of Petrology* **48**, 1793–1812. https://doi.org/10.1093/petrology/egm038.

Chiarabba, C., Amato, A., Boschi, E. & Barberi, F. (2000). Recent seismicity and tomographic modeling of the Mount Etna plumbing system. *Journal of Geophysical Research* **105**, 10923–10938. https://doi.org/10.1029/1999JB900427.

Chiarabba, C., De Gori, P. & Patanè, D. (2004). The Mt. Etna plumbing system: the contribution of seismic tomography. *Mt. Etna: Volcano Laboratory* **143**, 191–204. https://doi.org/10.1029/143GM12.

Chiodini, G., Caliro, S., Aiuppa, A., Avino, R., Granieri, D., Moretti, R. & Parello, F. (2011). First 13C/12C isotopic characterisation of volcanic plume CO2. *Bulletin of Volcanology* **73**, 531–542. https://doi.org/10.1007/s00445-010-0423-2.

Clocchiatti, R., Joron, J. L. & Treuil, M. (1988). The role of selective alkali contamination in the evolution of recent historic lavas of Mt. Etna. *Journal of Volcanology and Geothermal Research* **34**, 241–249. https://doi.org/10.1016/0377-0273(88)90036-4.

Clocchiatti, R., Schiano, P., Ottolini, L. & Bottazzi, P. (1998). Earlier alkaline and transitional magmatic pulsation of Mt Etna volcano. *Earth and Planetary Science Letters* **163**, 399–407. https://doi.org/10.1016/S0012-821X(98)00170-8.

Clocchiatti, R., Condomines, M., Guénot, N. & Tanguy, J. C. (2004). Magma changes at Mount Etna: the 2001 and 2002-2003 eruptions. *Earth and Planetary Science Letters* **226**, 397–414. https://doi.org/10.1016/j.epsl.2004.07.039.

Condomines, M., Tanguy, J. C. & Michaud, V. (1995). Magma dynamics at Mt Etna: constraints from U-Th-Ra-Pb radioactive disequilibria and Sr isotopes in historical lavas. *Earth and Planetary Science Letters* **132**, 25–41. https://doi.org/10.1016/0012-821X(95)00052-E.

Correale, A., Paonita, A., Martelli, M., Rizzo, A., Rotolo, S. G., Corsaro, R. A. & Di Renzo, V. (2014). A two-component mantle source feeding Mt. Etna magmatism: Insights from the geochemistry of primitive magmas. *Lithos* **184–187**, 243–258, https://doi.org/10.1016/j.lithos.2013.10.038.

Corsaro, R. A. & Métrich, N. (2016). Chemical heterogeneity of Mt. Etna magmas in the last 15 ka. Inferences on their mantle sources. *Lithos* **252–253**, 123–134.

Corsaro, R. A. & Miraglia, L. (2005). Dynamics of 2004–2005 Mt. Etna effusive eruption as inferred from petrologic monitoring. *Geophysical Research Letters* **32**, 1–5. https://doi.org/10.1029/2005gl022347.

Corsaro, R. A. & Miraglia, L. (2014). The transition from summit to flank activity at Mt. Etna, Sicily (Italy): inferences from the petrology of products erupted in 2007-2009. *Clinical and Laboratory Standards Institute (Series)* **275**, 51–60. https://doi.org/10.1016/j.jvolgeores.2014.02.009.

Corsaro, R. A. & Pompilio, M. (2004a). Dynamics of magmas at Mount Etna. *Mt. Etna: Volcano Laboratory* **143**, 91–110. https://doi.org/10.1029/143GM07.

Corsaro, R. A. & Pompilio, M. (2004b). Buoyancy-controlled eruption of magmas at Mt Etna. *Terra Nova* **16**, 16–22. https://doi.org/10.1046/j.1365-3121.2003.00520.x.

Corsaro, R. A. & Pompilio, M. (2004c). Magma dynamics in the shallow plumbing system of Mt. Etna as recorded by compositional variations in volcanics of recent summit activity (1995-1999). *Journal of Volcanology and Geothermal Research* **137**, 55–71. https://doi.org/10.1016/j.jvolgeores.2004.05.008.

Corsaro, R. A., Cristofolini, R. & Patanè, L. (1996). The 1669 eruption at Mount Etna: chronology, petrology and geochemistry, with inferences on the magma sources and ascent mechanisms. *Bulletin of Volcanology* **58**, 348–358. https://doi.org/10.1007/s004450050144.

Corsaro, R. A., Miraglia, L. & Pompilio, M. (2007). Petrologic evidence of a complex plumbing system feeding the July-august 2001 eruption of Mt. Etna, Sicily, Italy. *Bulletin of Volcanology* **69**, 401–421. https://doi.org/10.1007/s00445-006-0083-4.

Corsaro, R. A., Civetta, L., Di Renzo, V. & Miraglia, L. (2009). Petrology of lavas from the 2004-2005 flank eruption of Mt. Etna, Italy: inferences on the dynamics of magma in the shallow plumbing system. *Bulletin of Volcanology* **71**, 781–793. https://doi.org/10.1007/s00445-009-0264-z.

Corsaro, R. A., Di Renzo, V., Distefano, S., Miraglia, L. & Civetta, L. (2013). Relationship between petrologic processes in the plumbing system of Mt. Etna and the dynamics of the eastern flank from 1995 to 2005. *Clinical and Laboratory Standards Institute (Series)* **251**, 75–89. https://doi.org/10.1016/j.jvolgeores.2012.02.010.

Coulson, I. M., Stuart, F. M. & MacLean, N. J. (2011). Assessing the link between mantle source and sub-volcanic plumbing in the petrology of basalts from the 2001 and 2002/2003 eruptions of Mount Etna, Sicily: evidence from geochemical and helium isotope data. *Lithos* **123**, 254–261. https://doi.org/10.1016/j.lithos.2010.11.013.

Cristofolini, R., Ghisetti, F., Scarpa, R. & Vezzani, L. (1985). Character of the stress field in the Calabrian arc and southern Apennines (Italy) as deduced by geological, seismological and volcanological information. *Tectonophysics* **117**, 39–58. https://doi.org/10.1016/0040-1951(85)90235-5.

De Beni, E., Branca, S., Coltelli, M., Groppelli, G. & Wijbrans, J. R. (2011). $^{40}Ar/^{39}Ar$ isotopic dating of Etna volcanic succession. *Italian Journal of Geosciences* **130**, 292–305.

Deegan, F. M., Troll, V. R., Freda, C., Misiti, V., Chadwick, J. P., McLeod, C. L. & Davidson, J. P. (2010). Magma-carbonate interaction processes and associated CO_2 release at Merapi volcano, Indonesia: insights from experimental petrology. *Journal of Petrology* **51**, 1027–1051. https://doi.org/10.1093/petrology/egq010.

Del Carlo, P. & Pompilio, M. (2004). The relationship between volatile content and the eruptive style of basaltic magma: the Etna case. *Annals of Geophysics* **47**, 1–10.

Del Moro, A., Fulignati, P., Marianelli, P. & Sbrana, A. (2001). Magma contamination by direct wall rock interaction: constraints from xenoliths from the walls of a carbonate-hosted magma chamber (Vesuvius 1944 eruption). *Journal of Volcanology and Geothermal Research* **112**, 15–24. https://doi.org/10.1016/S0377-0273(01)00231-1.

Dewey, J. F., Helman, M. L., Turco, E., Hutton, D. H. W. & Knott, S. D. (1989). Kinematics of the western Mediterranean. *Alpine Tectonics* **45**, 265–283. https://doi.org/10.1144/GSL.SP.1989.045.01.15.

Di Rocco, T., Freda, C., Gaeta, M., Mollo, S. & Dallai, L. (2012). Magma chambers emplaced in carbonate substrate: Petrogenesis of skarn and cumulate rocks and implications for CO_2 degassing in volcanic areas. *Journal of Petrology* **53**, 2307–2332. https://doi.org/10.1093/petrology/egs051.

Erdmann, S., Scaillet, B. & Kellett, D. A. (2010). Xenocryst assimilation and formation of peritectic crystals during magma contamination: an experimental study. *Clinical and Laboratory Standards Institute (Series)* **198**, 355–367. https://doi.org/10.1016/j.jvolgeores.2010.10.002.

Ferlito, C., Viccaro, M. & Cristofolini, R. (2008). Volatile-induced magma differentiation in the plumbing system of Mt. Etna volcano (Italy): evidence from glass in tephra of the 2001 eruption. *Bulletin of Volcanology* **70**, 455–473. https://doi.org/10.1007/s00445-007-0149-y.

Ferlito, C., Viccaro, M. & Cristofolini, R. (2009). Volatile-rich magma injection into the feeding system during the 2001 eruption of Mt. Etna (Italy): its role on explosive activity and change in rheology of lavas. *Bulletin of Volcanology* **71**, 1149–1158. https://doi.org/10.1007/s00445-009-0290-x.

Ferlito, C., Viccaro, M., Nicotra, E. & Cristofolini, R. (2012). Regimes of magma recharge and their control on the eruptive behaviour during the period 2001–2005 at Mt. Etna volcano. *Bulletin Volcanologique* **74**, 533–543. https://doi.org/10.1007/s00445-011-0537-1.

Freda, C., Gaeta, M., Misiti, V., Mollo, S., Dolfi, D. & Scarlato, P. (2008). Magma-carbonate interaction: an experimental study on ultrapotassic rocks from Alban Hills (Central Italy). *Lithos* **101**, 397–415. https://doi.org/10.1016/j.lithos.2007.08.008.

Furlong, K. & Myers, J. (1985). Thermal-mechanical modeling of the role of thermal stresses and stoping in magma contamination. *Journal of Volcanology and Geothermal Research* **24**, 179–191. https://doi.org/10.1016/0377-0273(85)90032-0.

Gennaro, E., Iacono-Marziano, G., Paonita, A., Rotolo, S. G., Martel, C., Rizzo, A. L., Pichavant, M. & Liotta, M. (2019). Melt inclusions track melt evolution and degassing of Etnean magmas in the last 15 ka. *Lithos* **324-325**, 716–732. https://doi.org/10.1016/j.lithos.2018.11.023.

Ghiorso, M. S. & Gualda, G. A. R. (2015). An H_2O–CO_2 mixed fluid saturation model compatible with rhyolite-MELTS. *Contributions to Mineralogy and Petrology* **169**, 1–30.

Ghiorso, M. S. & Sack, R. O. (1995). Chemical mass transfer in magmatic processes IV. A revised and internally consistent thermodynamic model for the interpolation and extrapolation of liquid-solid equilibria in magmatic systems at elevated temperatures and pressures. *Contributions to Mineralogy and Petrology* **119**, 197–212. https://doi.org/10.1007/BF00307281.

Ghiorso, M. S., Hirschmann, M. M., Reiners, P. W. & Kress, V. C. (2002). The pMELTS: a revision of MELTS for improved calculation of phase relations and major element partitioning related to partial melting of the mantle to 3 GPa. *Geochemistry, Geophysics, Geosystems* **3**, 1–35. https://doi.org/10.1029/2001GC000217.

Giacomoni, P. P., Coltorti, M., Bryce, J. G., Fahnestock, M. F. & Guitreau, M. (2016). Mt. Etna plumbing system revealed by combined textural, compositional, and thermobarometric studies in clinopyroxenes. *Contributions to Mineralogy and Petrology* **171**, 1–15.

Giuffrida, M. & Viccaro, M. (2017). Three years (2011–2013) of eruptive activity at Mt. Etna: working modes and timescales of the modern volcano plumbing system from micro-analytical studies of crystals. *Earth-Science Reviews* **171**, 289–322. https://doi.org/10.1016/j.earscirev.2017.06.003.

Giuffrida, M., Cardone, M., Zuccarello, F. & Viccaro, M. (2023). Etna 2011-2022: discoveries from a decade of activity at the volcano. *Earth-Science Reviews* **245**, 104563. https://doi.org/10.1016/j.earscirev.2023.104563.

Goff, F., Janik, C. J., Delgado, H., Werner, C., Counce, D., Stimac, J. A., Siebe, C., Love, S. P., Williams, S. N., Fischer, T. & Johnson, L. (1998). Geochemical surveillance of magmatic volatiles at Popocatépetl volcano, Mexico. *Geological Society of America Bulletin* **110**, 0695–0710. https://doi.org/10.1130/0016-7606(1998)110<0695:GSOMVA>2.3.CO;2.

Goff, F., Love, S. P., Warren, R. G., Counce, D., Obenholzner, J., Siebe, C. & Schmidt, S. C. (2001). Passive infrared remote sensing evidence for large, intermittent CO_2 emissions at Popocatépetl volcano, Mexico. *Chemical Geology* **177**, 133–156. https://doi.org/10.1016/S0009-2541(00)00387-9.

Grasso, M. & Lentini, F. (1982). Sedimentary and tectonic evolution of the eastern Hyblean plateau (southeastern Sicily) during late cretaceous to quaternary time. *Paleogeography, Paleoclimatology, Paleoecology* **39**, 261–280. https://doi.org/10.1016/0031-0182(82)90025-6.

Gualda, G. A. R., Ghiorso, M. S., Lemons, R. V. & Carley, T. L. (2012). Rhyolite-MELTS: a modified calibration of MELTS optimized for silica-rich, fluid-bearing magmatic systems. *Journal of Petrology* **53**, 875–890. https://doi.org/10.1093/petrology/egr080.

Heap, M. J., Mollo, S., Vinciguerra, S., Lavallée, Y., Hess, K. U., Dingwell, D. B., Baud, P. & Iezzi, G. (2013). Thermal weakening of the carbonate basement under Mt. Etna volcano (Italy): implications for volcano instability. *Clinical and Laboratory Standards Institute (Series)* **250**, 42–60. https://doi.org/10.1016/j.jvolgeores.2012.10.004.

Heinonen, J. S., Luttinen, A. V., Spera, F. J. & Bohrson, W. A. (2019). Deep open storage and shallow closed transport system for a continental flood basalt sequence revealed with magma chamber simulator. *Contributions to Mineralogy and Petrology* **174**. https://doi.org/10.1007/s00410-019-1624-0.

Heinonen, J. S., Bohrson, W. A., Spera, F. J., Brown, G. A., Scruggs, M. A. & Adams, J. V. (2020). Diagnosing open-system magmatic processes using the magma chamber simulator (MCS): part II—trace elements and isotopes. *Contributions to Mineralogy and Petrology* **175**. https://doi.org/10.1007/s00410-020-01718-9.

Iacono Marziano, G., Gaillard, F. & Pichavant, M. (2007). Limestone assimilation and the origin of CO_2 emissions at the Alban Hills (Central Italy): constraints from experimental petrology. *Journal of Volcanology and Geothermal Research* **166**, 91–105. https://doi.org/10.1016/j.jvolgeores.2007.07.001.

Iacono Marziano, G., Gaillard, F. & Pichavant, M. (2008). Limestone assimilation by basaltic magmas: an experimental re-assessment and application to Italian volcanoes. *Contributions to Mineralogy and Petrology* **155**, 719–738. https://doi.org/10.1007/s00410-007-0267-8.

Iacono Marziano, G., Gaillard, F., Scaillet, B., Pichavant, M. & Chiodini, G. (2009). Role of non-mantle CO_2 in the dynamics of volcano degassing: the Mount Vesuvius example. *Geology* **37**, 319–322. https://doi.org/10.1130/G25446A.1.

Jolis, E. M., Freda, C., Troll, V. R., Deegan, F. M., Blythe, L. S., McLeod, C. L. & Davidson, J. P. (2013). Experimental simulation of magma-carbonate interaction beneath Mt. Vesuvius, Italy. *Contributions to Mineralogy and Petrology* **166**, 1335–1353. https://doi.org/10.1007/s00410-013-0931-0.

Jolis, E. M., Troll, V. R., Harris, C., Freda, C., Gaeta, M., Orsi, G. & Siebe, C. (2015). Skarn xenolith record crustal CO_2 liberation during Pompeii and Pollena eruptions, Vesuvius volcanic system, Central Italy. *Chemical Geology* **415**, 17–36. https://doi.org/10.1016/j.chemgeo.2015.09.003.

Joron, J. L. & Treuil, M. (1984). Étude géochemique et pétrogenèse des laves de l'Etna, Sicile, Italie. *Bulletin of Volcanology* **47**, 1125–1144. https://doi.org/10.1007/BF01952368.

Kahl, M., Chakraborty, S., Costa, F. & Pompilio, M. (2011). Dynamic plumbing system beneath volcanoes revealed by kinetic modeling, and the connection to monitoring data: an example from Mt. Etna. *Earth and Planetary Science Letters* **308**, 11–22. https://doi.org/10.1016/j.epsl.2011.05.008.

Kahl, M., Chakraborty, S., Costa, F., Pompilio, M., Liuzzo, M. & Viccaro, M. (2013). Compositionally zoned crystals and real-time degassing data reveal changes in magma transfer dynamics during the 2006 summit eruptive episodes of Mt. Etna. *Bulletin of Volcanology* **75**, 1–14. https://doi.org/10.1007/s00445-013-0692-7.

Kahl, M., Chakraborty, S., Pompilio, M. & Costa, F. (2015). Constraints on the nature and evolution of the magma plumbing system of Mt. Etna volcano (1991-2008) from a combined thermodynamic and kinetic modelling of the compositional record of minerals. *Journal of Petrology* **56**, 2025–2068. https://doi.org/10.1093/petrology/egv063.

Kahl, M., Viccaro, M., Ubide, T., Morgan, D. J. & Dingwell, D. B. (2017). A branched magma feeder system during the 1669 eruption of Mt Etna: evidence from a time-integrated study of zoned olivine phenocryst populations. *Journal of Petrology* **58**, 443–472. https://doi.org/10.1093/petrology/egx022.

Kamenetsky, V. S., Pompilio, M., Métrich, N., Sobolev, A. V., Kuzmin, D. V. & Thomas, R. (2007). Arrival of extremely volatile-rich high-mg magmas changes explosivity of Mount Etna. *Geology* **35**, 255–258. https://doi.org/10.1130/G23163A.1.

La Delfa, S., Patanè, G., Clocchiatti, R., Joron, J. L. & Tanguy, J. C. (2001). Activity of Mount Etna preceding the February 1999 fissure eruption: inferred mechanism from seismological and geochemical data. *Journal of Volcanology and Geothermal Research* **105**, 121–139. https://doi.org/10.1016/S0377-0273(00)00249-3.

Lanzafame, G., Neri, M., Acocella, V., Billi, A., Funiciello, R. & Giordano, G. (2003). Structural features of the July-august 2001 Mount Etna eruption: evidence for a complex magma supply system. *Journal of the Geological Society* **160**, 531–544. https://doi.org/10.1144/0016-764902-151.

Le Bas, M. J. L., Le Maitre, R. W. L., Streckeisen, A. & Zanettin, B. (1986). A Chemical Classification of Volcanic Rocks Based on the Total Alkali-Silica Diagram. *Journal of Petrology* **27**, 745–750. https://doi.org/10.1093/petrology/27.3.745.

Le Maitre, R. W. (1989). *A Classification of Igneous Rocks and Glossary of Terms*. Blackwell.

Lentini, F. (1982). The geology of Mt. Etna basement. *Memorie della Societá geologica italiana* **23**, 7–25.

Lentini, F., Carbone, S. & Guarnieri, P. (2006). Collisional and postcollisional tectonics of the Apenninic-Maghrebian orogen (southern Italy). *Geological Society of America Special Paper* **409**, 57–81. https://doi.org/10.1130/2006.2409(04).

Loddo, M., Patella, D., Quarto, R., Ruina, G., Tramacere, A. & Zito, G. (1989). Application of gravity and deep dipole geoelectrics in the volcanic area of Mt. Etna (Sicily). *Journal of Volcanology and Geothermal Research* **39**, 17–39. https://doi.org/10.1016/0377-0273(89)90018-8.

Magee, R., Ubide, T. & Caulfield, J. (2021). Days to weeks of syn-eruptive magma interaction: high-resolution geochemistry of the 2002-03 branched eruption at Mount Etna. *Earth and Planetary Science Letters* **565**, 116904. https://doi.org/10.1016/j.epsl.2021.116904.

Marty, B., Trull, T., Lussiez, P., Basile, I. & Tanguy, J. C. (1994). He, Ar, O, Sr and Nd isotope constraints on the origin and evolution of Mount Etna magmatism. *Earth and Planetary Science Letters* **126**, 23–39. https://doi.org/10.1016/0012-821X(94)90240-2.

McArthur, J. M., Howarth, R. J. & Bailey, T. R. (2001). Strontium isotope stratigraphy: LOWESS version 3: best fit to the marine Sr-isotope curve for 0–509 ma and accompanying look-up table for deriving numerical age. *The Journal of Geology* **109**, 155–170. https://doi.org/10.1086/319243.

Métrich, N. & Rutherford, M. J. (1998). Low pressure crystallization paths of H_2O-saturated basaltic-hawaiitic melts from Mt Etna: implications for open-system degassing of basaltic volcanoes. *Geochimica et Cosmochimica Acta* **62**, 1195–1205. https://doi.org/10.1016/S0016-7037(98)00048-9.

Métrich, N., Allard, P., Spilliaert, N., Andronico, D. & Burton, M. R. (2004). 2001 flank eruption of the alkali- and volatile-rich primitive basalt responsible for Mount Etna's evolution in the last three

decades. *Earth and Planetary Science Letters* **228**, 1–17. https://doi.org/10.1016/j.epsl.2004.09.036.

Michaud, V. (1995). Crustal xenoliths in recent hawaiites from Mount Etna, Italy: evidence for alkali exchanges during magma-wall rock interaction. *Chemical Geology* **122**, 21–42. https://doi.org/10.1016/0009-2541(94)00133-S.

Mikes, T., Dunkl, I., Frisch, W. & von Eynatten, H. (2006). Geochemistry of Eocene flysch sandstones in the NW external Dinarides. *Acta Geologica Hungarica* **49**, 103–124. https://doi.org/10.1556/AGeol.49.2006.2.2.

Mollo, S., Gaeta, M., Freda, C., Di Rocco, T., Misiti, V. & Scarlato, P. (2010). Carbonate assimilation in magmas: a reappraisal based on experimental petrology. *Lithos* **114**, 503–514. https://doi.org/10.1016/j.lithos.2009.10.013.

Moretti, R., Métrich, N., Arienzo, I., Di Renzo, V., Aiuppa, A. & Allard, P. (2018). Degassing vs. eruptive styles at Mt. Etna volcano. (Sicily, Italy). Part I: volatile stocking, gas fluxing, and the shift from low-energy to highly explosive basaltic eruptions. *Chemical Geology* **482**, 1–17. https://doi.org/10.1016/j.chemgeo.2017.09.017.

Murru, M., Montuori, C., Wyss, M. & Privitera, E. (1999). The locations of magma chambers at Mt. Etna, Italy, mapped by b-values. *Geophysical Research Letters* **26**, 2553–2556. https://doi.org/10.1029/1999GL900568.

Nelson, K. (2015). Timing and *Source* of Alkali Enrichment at Mt. Etna, Sicily: Constraints from Clinopyroxene Geobarometry and *In Situ* Sr Isotope Data. *All Master's Theses* 276 p. https://digitalcommons.cwu.edu/etd/276.

Neri, M., Acocella, V. & Behncke, B. (2004). The role of the Pernicana fault system in the spreading of Mt. Etna (Italy) during the 2002-2003 eruption. *Bulletin of Volcanology* **66**, 417–430. https://doi.org/10.1007/s00445-003-0322-x.

Nicotra, E. & Viccaro, M. (2012). Unusual magma storage conditions at Mt. Etna (southern Italy) as evidenced by plagioclase megacryst-bearing lavas: implications for the plumbing system geometry and summit caldera collapse. *Bulletin of Volcanology* **74**, 795–815. https://doi.org/10.1007/s00445-011-0566-9.

Pappalardo, L., Piochi, M., D'Antonio, M., Civetta, L. & Petrini, R. (2002). Evidence for multi-stage magmatic evolution during the past 60 kyr at Campi Flegrei (Italy) deduced from Sr, Nd and Pb isotope data. *Journal of Petrology* **43**, 1415–1434. https://doi.org/10.1093/petrology/43.8.1415.

Patanè, D., Aliotta, M., Cannata, A., Cassisi, C., Coltelli, M., Di Grazia, G., Montalto, P. & Zuccarello, L. (2011). Interplay between tectonics and Mount Etna's volcanism: insights into the geometry of the plumbing system. *New Frontiers in Tectonic Research - At the Midst of Plate Convergence* **364**. https://doi.org/10.5772/23503.

Pedley, H. M. & Grasso, M. (1992). Miocene syntectonic sedimentation along the western margins of the Hyblean-Malta platform: a guide to plate margin processes in the Central Mediterranean. *Journal of Geodynamics* **15**, 19–37. https://doi.org/10.1016/0264-3707(92)90004-C.

Salem, L. C., Edmonds, M., Corsaro, R. A. & Maclennan, J. (2019). Carbon dioxide in geochemically heterogeneous melt inclusions from Mount Etna, Italy. *Geochemistry, Geophysics, Geosystems* **20**, 3150–3169. https://doi.org/10.1029/2018GC008027.

Schellart, W. P. (2010). Mount Etna–Iblean volcanism caused by rollback-induced upper mantle upwelling around the Ionian slab edge: An alternative to the plume model. *Geology* **38**, 691–694. https://doi.org/10.1130/g31037.1.

Schiano, P., Clocchiatti, R., Ottolini, L. & Busà, T. (2001). Transition of Mount Etna lavas from a mantle-plume to an island-arc magmatic source. *Nature* **412**, 900–904. https://doi.org/10.1038/35091056.

Sharp, A. D. L., Davis, P. M. & Gray, F. (1980). A low velocity zone beneath Mount Etna and magma storage. *Nature* **287**, 587–591. https://doi.org/10.1038/287587a0.

Spera, F. J. & Bohrson, W. A. (2001). Energy-constrained open-system magmatic processes I: general model and energy-constrained assimilation and fractional crystallization (EC-AFC) formulation. *Journal of Petrology* **42**, 999–1018. https://doi.org/10.1093/petrology/42.5.999.

Spilliaert, N., Allard, P., Métrich, N. & Sobolev, A. V. (2006). Melt inclusion record of the conditions of ascent, degassing, and extrusion of volatile-rich alkali basalt during the powerful 2002 flank eruption of Mount Etna (Italy). *Journal of Geophysical Research* **111**, 1–19. https://doi.org/10.1029/2005JB003934.

Tanguy, J. C. & Clocchiatti, R. (1984). The Etnean lavas, 1977-1983: petrology and mineralogy. *Bulletin of Volcanology* **47**, 879–894. https://doi.org/10.1007/BF01952349.

Tanguy, J. C. & Kieffer, G. (1976). The 1974 eruption of Mount Etna. *Bulletin of Volcanology* **40**, 239–252. https://doi.org/10.1007/BF02597566.

Tanguy, J. C., Condomines, M. & Kieffer, G. (1997). Evolution of the Mount Etna magma: constraints on the present feeding system and eruptive mechanism. *Journal of Volcanology and Geothermal Research* **75**, 221–250. https://doi.org/10.1016/S0377-0273(96)00065-0.

Tibaldi, A. & Groppelli, G. (2002). Volcano-tectonic activity along structures of the unstable NE flank of Mt. Etna (Italy) and their possible origin. *Journal of Volcanology and Geothermal Research* **115**, 277–302. https://doi.org/10.1016/S0377-0273(01)00305-5.

Tonarini, S., Armienti, P., D'Orazio, M., Innocenti, F., Pompilio, M. & Petrini, R. (1995). Geochemical and isotopic monitoring of Mt. Etna 1989-1993 eruptive activity: bearing on the shallow feeding system. *Journal of Volcanology and Geothermal Research* **64**, 95–115. https://doi.org/10.1016/0377-0273(94)00039-J.

Tonarini, S., Armienti, P., D'Orazio, M. & Innocenti, F. (2001). Subduction-like fluids in the genesis of Mt. Etna magmas: evidence from boron isotopes and fluid mobile elements. *Earth and Planetary Science Letters* **192**, 471–483. https://doi.org/10.1016/S0012-821X(01)00487-3.

Trigila, R., Spera, F. J. & Aurisicchio, C. (1990). The 1983 Mount Etna eruption: thermochemical and dynamical inferences. *Contributions to Mineralogy and Petrology* **104**, 594–608. https://doi.org/10.1007/BF00306667.

Ubide, T. & Kamber, B. S. (2018). Volcanic crystals as time capsules of eruption history. *Nature Communications* **9**, 1–12. https://doi.org/10.1038/s41467-017-02274-w.

Viccaro, M. & Cristofolini, R. (2008). Nature of mantle heterogeneity and its role in the short-term geochemical and volcanological evolution of Mt. Etna (Italy). *Lithos* **105**, 272–288. https://doi.org/10.1016/j.lithos.2008.05.001.

Viccaro, M. & Zuccarello, F. (2017). Mantle ingredients for making the fingerprint of Etna alkaline magmas: implications for shallow partial melting within the complex geodynamic framework of eastern Sicily. *Journal of Geodynamics* **109**, 10–23. https://doi.org/10.1016/j.jog.2017.06.002.

Viccaro, M., Ferlito, C., Cortesogno, L., Cristofolini, R. & Gaggero, L. (2006). Magma mixing during the 2001 event at Mount Etna (Italy): effects on the eruptive dynamics. *Journal of Volcanology and Geothermal Research* **149**, 139–159. https://doi.org/10.1016/j.jvolgeores.2005.06.004.

Viccaro, M., Giacomoni, P. P., Ferlito, C. & Cristofolini, R. (2010). Dynamics of magma supply at Mt. Etna volcano (southern Italy)

as revealed by textural and compositional features of plagioclase phenocrysts. *Lithos* **116**, 77–91. https://doi.org/10.1016/j.lithos.2009.12.012.

Viccaro, M., Nicotra, E., Millar, I. L. & Cristofolini, R. (2011). The magma source at Mount Etna volcano: perspectives from the Hf isotope composition of historic and recent lavas. *Chemical Geology* **281**, 343–351. https://doi.org/10.1016/j.chemgeo.2010.12.020.

Viccaro, M., Calcagno, R., Garozzo, I., Giuffrida, M. & Nicotra, E. (2015). Continuous magma recharge at Mt. Etna during the 2011 – 2013 period controls the style of volcanic activity and compositions of erupted lavas. *Mineralogy and Petrology* **109**, 67–83. https://doi.org/10.1007/s00710-014-0352-4.

Viccaro, M., Barca, D., Bohrson, W. A., D'Oriano, C., Giuffrida, M., Nicotra, E. & Pitcher, B. W. (2016). Crystal residence times from trace element zoning in plagioclase reveal changes in magma transfer dynamics at Mt. Etna during the last 400 years. *Lithos* **248-251**, 309–323. https://doi.org/10.1016/j.lithos.2016.02.004.

Yellin-Dror, A., Grasso, M., Ben-Avraham, Z. & Tibor, G. (1997). The subsidence history of the northern Hyblean plateau margin, southeastern Sicily. *Tectonophysics* **282**, 277–289. https://doi.org/10.1016/S0040-1951(97)00228-X.

Zuccarello, F., Schiavi, F. & Viccaro, M. (2021). Magma dehydration controls the energy of recent eruptions at Mt. Etna volcano. *Terra Nova* **33**, 423–429. https://doi.org/10.1111/ter.12527.

Zuccarello, F., Schiavi, F. & Viccaro, M. (2022). The eruption run-up at Mt. Etna volcano: constraining magma decompression rates and their relationships with the final eruptive energy. *Earth and Planetary Science Letters* **597**, 117821. https://doi.org/10.1016/j.epsl.2022.117821.